FY17 Status Report: Research on Stress Corrosion Cracking of SNF Interim Storage Canisters

Spent Fuel and Waste Disposition

Prepared for
US Department of Energy
Spent Fuel and Waste Science and Technology

Eric Schindelholz, Charles Bryan, and Christopher Alexander

August 25, 2017

SFWD-SFWST-2017-000003
SAND2017-10338 R

DISCLAIMER

This information was prepared as an account of work sponsored by an agency of the U.S. Government. Neither the U.S. Government nor any agency thereof, nor any of their employees, makes any warranty, expressed or implied, or assumes any legal liability or responsibility for the accuracy, completeness, or usefulness, of any information, apparatus, product, or process disclosed, or represents that its use would not infringe privately owned rights. References herein to any specific commercial product, process, or service by trade name, trade mark, manufacturer, or otherwise, does not necessarily constitute or imply its endorsement, recommendation, or favoring by the U.S. Government or any agency thereof. The views and opinions of authors expressed herein do not necessarily state or reflect those of the U.S. Government or any agency thereof.

Sandia National Laboratories is a multimission laboratory managed and operated by National Technology and Engineering Solutions of Sandia, LLC., a wholly owned subsidiary of Honeywell International, Inc., for the U.S. Department of Energy's National Nuclear Security Administration under contract DE-NA0003525.

SUMMARY

This progress report describes work done in FY17 at Sandia National Laboratories (SNL) to assess the localized corrosion performance of container/cask materials used in the interim storage of spent nuclear fuel (SNF). Of particular concern is stress corrosion cracking (SCC), by which a through-wall crack could potentially form in a canister outer wall over time intervals that are shorter than possible dry storage times. Work in FY17 refined our understanding of the chemical and physical environment on canister surfaces, and evaluated the relationship between chemical and physical environment and the form and extent of corrosion that occurs. The SNL corrosion work focused predominantly on pitting corrosion, a necessary precursor for SCC, and process of pit-to-crack transition; it has been carried out in collaboration with university partners. SNL is collaborating with several university partners to investigate SCC crack growth experimentally, providing guidance for design and interpretation of experiments.

Work to define the chemical and physical environment that could develop by deliquescence of sea-salts on storage canister surfaces consisted of thermodynamic modeling and experimental work to evaluate brine compositions and properties (e.g., volume as a function of relative humidity). These parameters are important inputs for mechanistic models of localized corrosion, such as that developed by Chen and Kelly (2010), and for stress corrosion cracking. However, the thermodynamic calculations do not consider reactions between atmospheric gases and sea-salt aerosol particles, known as gas-to-particle conversion reactions, that can significantly modify salt and brine compositions. One such reaction that could occur when sea-salts initially deliquesce to form magnesium-chloride-rich brines is carbonation—absorption of CO_2 from the atmosphere, coupled with concomitant outgassing of HCl and precipitation of non-deliquescent magnesium carbonate. Experimental evaluation of $MgCl_2$ brine stability at canister-relevant RH and temperature conditions confirmed that this reaction can occur, and could lead to rapid dry-out of the deliquesced brine. While acidification reactions with other atmospheric gases (e.g., HNO_3, H_2SO_4) may play a larger role in natural systems, the carbonation reaction is bounding. In experimental systems containing small masses of salts and run for long periods of time, understanding the role of atmospheric reactions, including the carbonation reaction, is critical for proper interpretation of the results. Consideration of atmospheric exchange reactions is critical to understanding the long-term stability of deliquescent brines on heated canister surfaces, and to judging the relevance of long-term corrosion experimental work in confined-volume laboratory systems.

Finally, work by other researchers has suggested that corrosion may be more extreme in natural environments due to daily and seasonal variations in temperature and RH, especially if the RH variations cross the deliquescence RH of the salts. Sandia will evaluate the effects of cyclic variations experimentally. However, on canister surfaces, the diurnal variations in the ambient temperature and RH will be modified by the decay heat of the canister. In preparation to running corrosion experiments under cyclic conditions, one realistic cycle for canister surface temperature and RH has been identified, and will be used in future experiments.

Sandia also initiated several experiments evaluating pitting corrosion and SCC under conditions relevant to the canister surface. These experiments focus on identifying the role of environmental factors (temperature, RH, and salt load) on the rate and extent of pitting damage over time. The first experiment aims to quantify pitting rates and size distributions over time on 304 stainless steel coupons, as a function of temperature, RH, and salt load, and is being carried out in collaboration with Ohio State University. Data from early sample pulls has been collected, and interpretation is underway. Features associated with pits that serve as crack initiation sites are also being identified as means of understanding what conditions initiate cracking. A second set of experiments is evaluating the kinetics of cathodic reactions as a function of brine layer thickness, composition, and temperature, using a high-speed rotating disc electrode. These experiments will provide needed inputs to mechanistic models that evaluate the maximum possible pit size that can form under a given set of environmental conditions. A third suite of experiments is evaluating the effects of the corrosion reactions on the distribution and composition of

solutes in the cathode region on the metal surface. Existing mechanistic models for corrosion largely ignore these effects, which can have a huge effect on brine compositions in the cathode region, potentially changing the kinetics of the oxygen reduction reaction. However, these reactions may also serve to disperse solutes over the metal surface, helping individual sea-salt particles form a continuous brine film. Finally, in collaboration with the Colorado School of Mines, Sandia is evaluating the effect of stress on pit size and shape distributions and the extent of damage. This is being done by evaluating pitting in stress profiles on the side of 4-point bend specimens aged under similar environments as our coupon pitting experiments. Colorado School of Mines has modeled the stress profiles, while Sandia will characterize the electrochemical properties of the metal as a function of location (and stress level) on the samples. This will ultimately provide information on the likely location of pits that initiate SCC on canister surfaces.

All of these experiments will extend into FY18, along with new experiments that will evaluate pitting, crack initiation, and crack orientation on samples from the Sandia full-dimeter canister mockup. The mockup experiments will provide a critical link between the laboratory-scale coupon experiments and actual corrosion on a spent nuclear fuel storage canister surface.

ACKNOWLEDGEMENTS

The authors would like to acknowledge collaborators at the Colorado School of Mines, including Zhenzhen Yu, Xin Wu, and Scott Gordon, and at Ohio State University, including Jenifer Locke and Timothy Weirich. At Sandia, the authors thank Jason Taylor, Tony Ohlhausen, Chip Olson, and Liz Huffman.

This page is intentionally left blank.

CONTENTS

LIST OF FIGURES

LIST OF TABLES

ACRONYMS

AH	absolute humidity
CRIEPI	[Japanese] Central Research Institute of the Electric Power Industry
CSM	Colorado School of Mines
DOE	US Department of Energy
EDS	energy dispersive [X-ray] spectroscopy
EFRC	Energy Frontier Research Center
EPRI	Electric Power Research institute
FY	fiscal year
IC	ion chromatography
IRP	integrated research project
ISFSI	independent spent fuel storage installation
NRC	Nuclear Regulatory Commission
ORR	oxygen reduction reaction
OSU	Ohio State University
RH	relative humidity
SCC	stress corrosion cracking
SEM	scanning electron microscope
SFWST	spent fuel and waste science and technology
SNF	spent nuclear fuel
SNL	Sandia National Laboratory
T	temperature
TOF-SIMS	time-of-flight secondary ion mass spectrometry

This page is intentionally left blank.

SPENT FUEL AND WASTE SCIENCE AND TECHNOLOGY PROGRAM

RESEARCH ON STRESS CORROSION CRACKING OF SNF INTERIM STORAGE CANISTERS

1. INTRODUCTION

This progress report describes work being done at Sandia National Laboratories (SNL) to assess the localized corrosion performance of container materials used in the interim storage of spent nuclear fuel (SNF). Of particular concern is stress corrosion cracking (SCC), a mechanism by which a through-wall crack could potentially form in a storage canister over time intervals that are shorter than possible dry storage times. Developing an understanding of stress corrosion cracking (SCC) of interim storage containers has been indicated as a high priority data gap by the Department of Energy (DOE) (Hanson et al., 2012), the Electric Power Research Institute (EPRI, 2011), the Nuclear Waste Technical Review Board (NWTRB, 2010), and the Nuclear Regulatory Commission (NRC, 2012a; NRC, 2012b).

1.1 Background

In dry storage, SNF is commonly stored in welded stainless steel canisters enclosed in passively-ventilated overpacks. As outside air is advectively drawn through the overpacks, dust accumulates on the canister surfaces. Over time, as the SNF cools, the canister surface temperatures drop to the point that salts within that dust will deliquesce to form concentrated brines. If the salts contain aggressive species such as chloride, then the resulting brine can cause localized corrosion—pitting—to occur. If sufficient stresses are present, the pitting can eventually convert to SCC, which over time could penetrate the canister wall. The risk of corrosion and SCC is greatest in near-marine settings, where chloride-rich sea-salt aerosols are deposited on the canister surface.

A timeline for SCC of spent nuclear fuel canisters in dry storage is shown in Figure 1. Several important events and processes occur during the development of through-wall SCC, and understanding the timing of event initiation and rate of processes is critical to accurate evaluation of SCC penetration rates. These parameters are highly dependent upon the evolving physical and chemical environment on the canister surface, and on the canister material properties, including composition, surface finish, and weld-related microstructure and residual stress levels. SNL and several collaborators are working to understand these dependencies, and their effect on potential canister penetration rates by SCC. This information is critical to understanding the potential risk of canister failure during extended interim storage at reactor sites or at consolidated interim storage sites.

Immediately after placement into an overpack, canister surface temperatures are too high to permit salt deliquescence or even development of adsorbed water layers on salts, and localized corrosion cannot occur. Even after deliquescence, corrosion may be delayed for a time, although this period is likely to be insignificant relative to storage time intervals. This initial period is known as the incubation period, and is a function of the physical environment—the temperature, relative humidity (RH) and salt load on the canister surface. The chemical composition of the salt is also important, as it controls the RH at which deliquescence occurs. SNL is evaluating the physical conditions and the chemical environment on the canister surface, both prior to and after initiation of corrosion. Of particular interest is the long-term stability of brines formed by sea-salt deliquescence on the heated canister surface, and the effect of atmospheric exchange reactions and corrosion reactions.

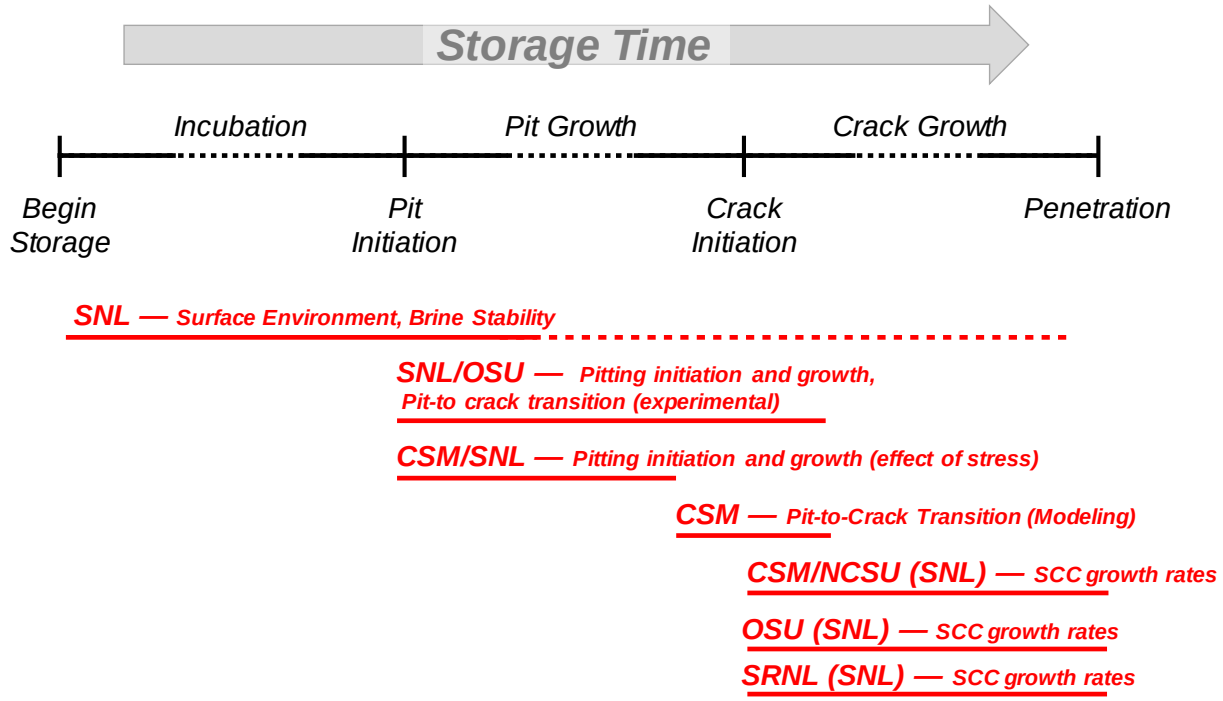

Figure 1. Time line for stress corrosion cracking, showing current experimental work being carried out by SNL and collaborators.

Once deliquescence occurs, if the deliquescent brine is chemically aggressive (e.g. chloride-rich), then pitting corrosion will initiate. Pitting initiation and pit growth rates, and possible limitations on pit growth, are strongly controlled by environmental factors such as temperature, RH, and salt load, but also by material properties, including composition, surface finish, microstructure, and stress level. SNL is collaborating with the Colorado School of Mines (CSM) as part of a DOE Integrated Research Project (IRP) to evaluate the effect of stress on pit growth rates, and is working with Ohio State University (OSU) to evaluate pit initiation and growth on unstrained samples with different surface finishes. Collaboration with OSU is through their WastePD Energy Frontier Research Center (EFRC). SNL is also evaluating the effect of brine composition on cathodic reaction rates in regions surrounding the pit, and also how those rates may change as corrosion reactions could affect the composition of the brine in the cathode region.

In the presence of tensile stresses, the current assumption is that pits that grow sufficiently large will eventually initiate SCC cracks. Existing models relate pit depth to crack initiation through the calculated crack tip stress intensity factor (e.g., Kondo, 1989; Turnbull et al., 2006). However, this approach must be implemented stochastically, and makes broad assumptions about the shape of the pit. To develop a more realistic relationship between pitting and crack initiation, SNL is working with OSU to experimentally evaluate conditions of pit to crack transition under controlled conditions. SNL will also evaluate pitting and crack initiation using a large weld sample from a full-diameter canister mockup that SNL has previously used to characterize weld residual stresses (Enos and Bryan, 2016).

Once a SCC crack initiates, the rate of crack growth will be controlled by the temperature and chemical environment, as well as, possibly, the salt surface load. The overall level of tensile stress is also important, combining with the depth of the crack to determine the crack tip stress intensity factor (Newman and Raju, 1979; Newman and Raju, 1981). SNL is working with colleagues at North Carolina State University as part of the CSM-led IRP to measure crack growth rates as a function of brine

composition. Also, SNL is collaborating with OSU to evaluate the effect of salt load on crack growth rates—to determine if the limited cathode areas associated with thin brine films limit crack growth rates or crack depth. Finally, SNL has provided input to Savannah River National Laboratory (SRNL), helping to define relevant conditions for crack initiation and growth testing. In each of these, SNL's role to date has been to help define testing conditions, but we will also support post-test characterization of the SCC cracks that form in several of the tests.

1.2 FY17 Tasks and Current Status

Prediction of SCC formation initiation and growth requires both (a) a statistical description of the inherently stochastic process of pit formation, growth and conversion to a SCC crack under conditions (material and surface environment) representative of fielded canisters and (b) a deterministic/mechanistic understanding of environment-material-electrochemical interrelationships. Purely statistical approaches provide a means of quantifying variability and uncertainty in material and surface condition, but cannot be confidently extrapolated beyond the range of conditions or the time interval under which the data were collected, without a mechanistic understanding of the processes involved. Mechanistic studies serve to inform and provide confidence in statistical extrapolation for prediction of these processes. Sandia, the IRP and other collaborators are pursuing both avenues for prediction of SCC behavior of used fuel nuclear waste containers at independent spent fuel storage installation (ISFSI) sites. Challenges common to both approaches are lack of data on canister surface environment, and an incomplete understanding of the relationships between environment, material, and corrosion response under field-relevant conditions. This challenge manifests itself in selection of appropriate environmental and material inputs for models, development of experiments relating environment/material to damage rates and distributions, and utilization of experimental data as inputs and benchmarking tools for predictive models.

Efforts at SNL take advantage of unique combination of expertise and capabilities in geochemistry, surface science, metallurgy and electrochemistry to:

- Advance the quantitative definition of the physical and chemical environment on the surface of SNF interim storage canisters, and its temporal and spatial evolution to inform modeling and relevant laboratory experiments.
- Rigorously characterize the relationship between the surface environment and damage distributions and rates, with emphasis on electrochemical kinetics.
- Quantify the impact of materials variability (stress, strain, microstructure, surface finish) on electrochemical corrosion processes from pitting initiation to stress corrosion cracking.

These efforts will provide knowledge and data necessary for relating canister-relevant surface environments and material conditions to corrosion processes. This understanding will support efforts at Sandia and elsewhere to design and carry out relevant laboratory corrosion/SCC tests and to interpret the results of those tests. Ultimately, it will support improved modeling of storage canister performance during long-term interim storage.

Sandia research will focus on the three thrust areas listed above. Testing will be done at experimental conditions (e.g., salt loading, humidity, temperature) that bound expected canister surface conditions in marine coastal environments, which are expected to be the most severe case for SCC. Specific tasks initiated in FY 17 and in early FY18 are listed in Table 1, along with the current status of each task. Each of these will be discussed in detail in the remainder of this report.

Table 1. Status of Tasks in FY17 Work Plan.

Thrust	Task	Status
Definition of Surface Environment	Calculate seasonal/diurnal variations in surface environment (RH, T, brine) for typical marine site. (define conditions for planned varying-RH corrosion tests)	Completed.
	Experimentally test $MgCl_2$ brine stability under varying HCl/H_2SO_4 partial pressures	Initial tests completed, indicate $MgCl_2$ carbonation occurs at canister surface temperatures.
	Journal paper outline- review of surface conditions in marine environments (characteristics of sea-salt brines) in relation to corrosion	In progress.
Surface Environment-Damage Relationship	Benchmark Chen-Kelly maximum pit size model against existing literature data and identify model experimental input needs. (collaboration with R. Dingreville at SNL)	Literature search completed—available data limited and not useful for benchmarking model.
	Identify environmental conditions of interest for coupon-level pitting study based on lit. data, Chen-Kelly model, canister conditions and CSM experiments (collaboration with CSM, OSU)	Completed. Testing matrix defined.
	Demonstrate feasibility of high-throughput testing approach for coupon-level pitting statistics for one identified test condition (collaboration with OSU)	Long-term (2-year) pitting experiments started, one-week and one-month samples taken, and pitting characterized at OSU.
	Characterization of surface chemistry evolution on exposed coupon from pitting statistics tests, focusing on cathode signatures (collaboration with OSU)	Initial tests demonstrating method completed. Further work in progress.
	Initiate 1-year-plus experiment to evaluate effect of coupon size on evolution of pit distributions.	Experiment initiated, no samples taken yet.
	Evaluation of oxygen reduction kinetics in concentrated brines using rotating disc electrode: demonstrate method for one brine.	Method successfully tested. Matrix of tests evaluating the effect of brine composition and brine layer thickness developed. Tests in progress.
Material Variance-Damage Relationship	Map anodic and cathodic kinetics vs. stress to support electrochemical interpretation of atmospheric pitting behavior on a bend bar sample under study at CSM. (collaboration with CSM)	Samples delivered from CSM, construction and testing of 2-D electrochemical mapping device in progress.
	Initiate lab exposure of large canister mockup specimen to evaluate pitting and cracking frequency, and pit-to-crack transition for one test condition	Delayed due to funding limitations. Work restarted—currently developing a path forward for coating the large sample with salts.
Programmatic	Update SNL Research Plan outlining proposed FY18 and 19 activities, milestones and budget	Delayed until funding level has been clarified. Currently in progress.
	FY17 SFWST End-of-Year Level 2 Milestone: Status Report on S&T Corrosion Work at SNL	Completed.

2. CHARACTERIZATION OF THE CHEMICAL AND PHYSICAL ENVIRONMENT ON STORAGE CANISTER SURFACES

Current deterministic corrosion models (e.g., Engelhardt and Macdonald, 2004; Chen and Kelly, 2010; Macdonald and Engelhardt, 2010) approximate surface electrolytes as chemically and physically fixed in terms of composition, properties, and electrochemical kinetics. Furthermore, laboratory studies are often designed and interpreted without taking into account changes in electrolyte due to atmospheric exchange reactions or corrosion interactions, or are carried out under conditions that limit atmospheric exchange (e.g., in static systems with the RH controlled by salt solutions). This thrust aims to evaluate the chemical and physical properties of electrolytes under canister-relevant conditions. First, we have identified relevant temperature and RH conditions on canister surfaces, and quantified the typical response of these parameters to daily and seasonal swings in ambient temperature and RH. These data will be used to define experimental conditions for future corrosion testing under varying T and RH conditions chosen to simulate field-relevant conditions. These experiments will quantify the impact of daily and seasonal variations in T and RH on damage distributions and rates, and their linkage to underlying electrochemical corrosion processes. A second goal is to evaluate the interactions of deposited sea salt aerosols with atmospheric gas species in marine atmospheres (e.g., CO_2, HCl, H_2SO_4), that can result in considerable changes in chemistry and deliquescence properties and that have heretofore been ignored. Such atmospheric exchange reactions can affect electrolyte compositions and properties, and the corresponding corrosion response. Corrosion processes themselves will also affect brine composition, potentially leading to dry-out or to evolution to a less corrosive brine. SNL is evaluating this through geochemical modeling and experimental testing of the stability of sea-salt aerosols and deliquescent brines at conditions relevant to the canister surface.

Sandia's three goals for this thrust in FY17 are as follows:

- Prediction of canister surface T and RH profiles representative of the effects of diurnal and seasonal ambient atmospheric fluctuations, using weather data from a typical ISFSI site. This information will be used to inform testing protocols for systems run at varying T and RH.
- As an initial test of the potential effects of atmospheric exchange, experimentally evaluate $MgCl_2$ brine evolution due to coupled CO_2 absorption and HCl degassing at temperatures relevant to the heated canister surface.
- Through thermodynamic calculations and experimental measurements, evaluate the physical and chemical properties of brines formed by deliquescence of marine aerosols as a function of canister surface environment (T, RH, and salt load). Develop an outline for a journal article documenting these results. A later paper will evaluate the potential effects of atmospheric interactions on brine chemistry.

Each of these is discussed in more detail in the following sections.

2.1 Seasonal and Diurnal Variations in Canister Surface Environment.

For a SNF dry storage canister within its overpack, surface temperatures vary widely with location due to passive cooling by air flowing up through the overpack. Air entering the overpack through inlet vents near the base flows up and around the canister, becoming hotter as it moves upward. Canister surface temperatures are lowest near the inlet at the base and increase upwards. At any given location, canister surface temperatures are highest immediately after loading, and decrease over time as the fuel ages and the heat load drops.

At any given canister surface location and point in time, the temperature is a function of both the heat load and the temperature of the ambient air entering the overpack. This is because the efficiency of passive cooling is strongly a function of the ambient air temperature. Previous thermal modeling of canisters within their overpack indicates that the surface temperature varies nearly linearly with the ambient air temperature; to a reasonable approximation, a 1ºC increase in ambient air temperature equates to a 1ºC increase is canister surface temperature. Moreover, despite the canister thermal mass, the very efficient passive cooling means that canister surface temperatures change rapidly in response to changes in ambient air temperature. Hence, it is reasonable to assume that canister surface temperatures at any given location will track diurnal and seasonal variations the outside temperature, maintaining a fixed offset, or delta, due to the heating from the fuel.

The RH at any given canister surface location is a function of the surface temperature and absolute humidity (AH), or water content, of the incoming air. It, too varies diurnally and seasonally, both because of changes ambient air temperature and corresponding changes in canister surface temperature, and because of diurnal and seasonal changes in the AH of the ambient air.

Hence, canister surface temperatures and RH vary daily and seasonally as the outside air temperature and AH change. This can have major effects on the volume of deliquescent brine present and on the composition of the brine. In the extreme case, daily weather changes may cause the RH at the canister surface to fluctuate above and below the deliquescence RH for the deposited salts, causing the salts to dry out and re-wet on a daily basis. *Note all SNF canisters, as they cool, will pass through an interval when the periodic dry-out and rewetting of salts will occur in response to ambient weather fluctuations.*

Siegel et al. (2015) suggested that conditions of periodic dry-out are the most aggressive for corrosion initiation and growth, perhaps because of the formation of very concentrated brines as dry-out occurs. Some experimental studies have attempted to evaluate the effects of cyclical changes in RH and periodic dry-out on the extent and rate of corrosion (NRC, 2014; Siegel et al., 2015). However, these experiments did not cycle T and RH in a realistic manner or over a realistic range for field conditions. Under natural conditions, AH varies relatively little over the course of the day; changes in ambient RH are driven largely by changes in T. This means the T and RH correlate indirectly—higher temperatures correspond to lower RH values. On the canister surface, the temperature would be higher than ambient, but the same relationship would hold. Moreover, with increasing canister surface temperature, the maximum possible RH decreases, and the swing caused by daily temperature fluctuations narrows. Experimental studies run under cyclic conditions have not captured this relationship. For instance, the NRC (2014) evaluated pitting and SCC initiation under cyclic temperature and RH conditions, but utilized a system design where T and RH covaried directly—higher temperatures corresponded to higher RH values. Moreover, during the cycle, the AH varied by more than 12 g/m^3, a much higher range than is commonly observed in daily fluctuations at natural sites. Siegel et al. (2015) evaluated SCC crack growth in aluminum under cyclic RH conditions, but held the temperature constant and varied the RH from 40% to 90%, corresponding to an AH variation of over 15 g/m^3.

Finally, for both experiments, no attempt was made to ramp temperature and RH at rates that were typical of natural settings. If Siegel is correct that corrosion rate increases as brine concentration increases during the dry-out step, then it is clear that the rate of RH change is a critical parameter, especially if the goal is to compare corrosion rates determined by testing at constant RH with those determined under realistically varying conditions.

The goal of this task is to utilize real ISFSI site-specific weather data to develop a realistic model for coupled diurnal variations in T and RH on a heated canister surface. Specifically, we have identified conditions where the RH fluctuates on a daily cycle above and below the deliquescence RH for sea-salts, potentially resulting in daily dry-out and re-deliquescence. This temperature/RH cycle will be used in corrosion experiments to evaluate the effects of diurnal weather cycles on pitting and SCC.

To determine a realistic diurnal cycle in T and RH, weather data sets were examined, collected at the nearest airports to three different ISFSIs; San Onofre, Arkansas Nuclear 1, and Turkey Point (airport data sets are very complete, with data collected on an hourly schedule). Of these, the Arkansas Nuclear 1 data set was chosen for further analysis, because it exhibited both a high average AH and large daily temperature swings. A high average AH means that the deliquescence RH is reached at a higher temperature, important experimentally because higher T will speed corrosion and shorten necessary experiment times. Large daily temperature swings are also useful, and they result in larger RH swings, increasing the probability of finding a time interval in which the daily RH fluctuations intersect the deliquescence RH, resulting in dry-out and re-wetting.

Once the data set had been identified, different temperature offsets were applied to the ambient data to represent the heated canister surface, and a new RH was calculated at the higher temperature using the methods of Wagner and Pruß (2002). Examples of the results are in shown in Figure 2. In Figure 2a, the ambient temperature and relative humidity are provided for the entire year of 2013. A large seasonal fluctuation in temperature are obvious, and short-term (daily or day-to-day) fluctuations form a band about 20ºC wide. The range of RH values does not show a significant seasonal dependence, and short-term fluctuations define a broad band, as much as 70% wide. Calculated RH values for a temperature offset of 10ºC are shown in Figure 2b. The width of the T band does not change—it is simply offset 10ºC higher. The RH band is offset to much lower values and is also much narrower, only about 30% wide. Increasing the temperatures to 20ºC above ambient (Figure 2c) results in lower RH values and an even narrower band of RH values.

Figure 3 shows the same data sets, zooming in on 20 days in the summer, to illustrate daily T, RH, and AH fluctuations. In these data, the indirect correlation between temperature and RH is clear; when temperature rises, RH drops. This occurs because, as seen in Figure 3c, diurnal changes in AH are generally quite small, and for a constant AH, a rise in T forces in a drop in RH.

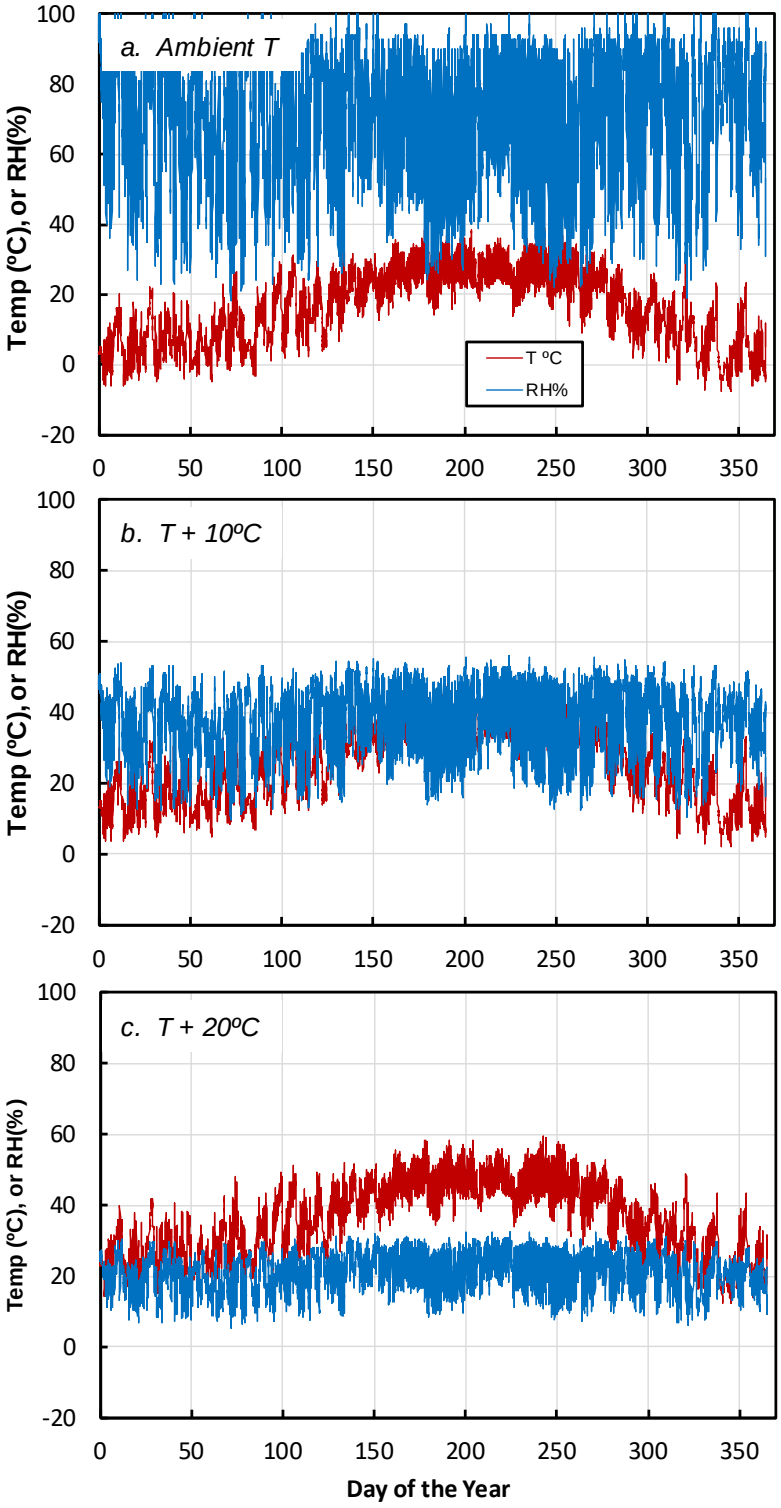

Figure 2. Effect of increasing canister surface T on surface RH, for Arkansas Nuclear 1 weather data. (a) ambient T; (b) ambient T+10ºC; (c) ambient T+20ºC.

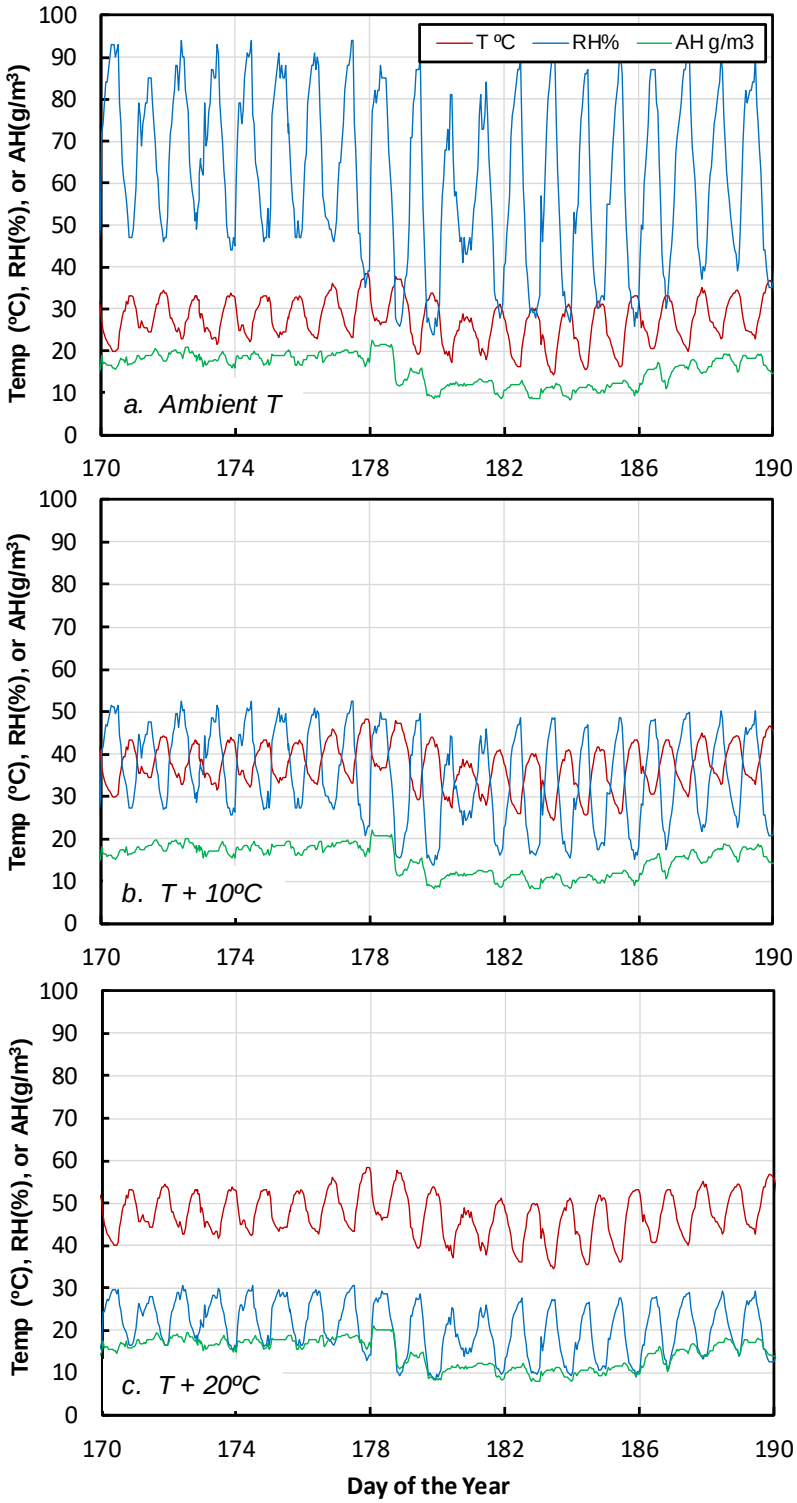

Figure 3. Effect of increasing T on RH, for Arkansas Nuclear 1 weather data, zooming in on 20 days in the summer. (a) ambient T; (b) ambient T+10ºC; (c) ambient T+20ºC.

In order to utilize a representative diurnal temperature and RH fluctuation in an experiment, a one-week section of the data in Figure 3, representing the time interval from 170 to 177 days, was fitted using Excel Solver with a repeating 24-hour cycle discretized into 2-hour intervals. Temperature and RH cycles were determined independently. The resulting cycles are given in Table 2, and the resulting fits are compared to the actual data in Figure 4. The 24-hours cycle fits the data well. Also shown in Figure 4 are AH values calculated from the paired temperature and RH values for the 24-hour cycle; again, the calculated values are consistent with the actual data.

Table 2. Best-Fit 24-Hour Cycle for Diurnal Weather Variations in Figure 3 (170-177 days).

Hour	Temp. ºC	RH, %
2	41.68	30.33
4	36.45	41.68
6	35.27	43.92
8	34.35	46.69
10	33.69	48.68
12	32.74	49.54
14	33.44	49.57
16	38.24	40.98
18	40.55	34.62
20	42.69	30.62
22	43.51	27.82
24	42.97	29.15

While independently fitting both T and RH yields the best fit to the data and captures the diurnal variations well over the 7-day period examined, this approach may be difficult to implement in an RH chamber because RH is strongly dependent on T, and varying them both simultaneously may not be possible, or may not yield the desired smooth transition from point to point. A simpler approach makes use of the fact the AH varies little over the 24-hour cycle (Figure 3c). Holding the AH constant at 17.5 g/m^3 while following the 24-hour temperature cycle in Table 2 yields an RH cycle that matches the temperature-adjusted weather data nearly as well as the best-fit RH curve (Figure 5). The diurnal variations are captured well, and overall shape of the curve matches the slow daily increases and decreases in RH. This is important because the transition periods have been identified as critical times, during which there appears to be an increase in corrosion rate (Siegel et al., 2015).

Finally, it should be obvious that many possible T and RH cycles exist that meet the criterion of intersecting the deliquescence RH on a daily basis. The cycle determined here is just one realistic choice, that can be readily implemented, because at least over the time interval evaluated, the day-to-day fluctuations are highly regular and can be duplicated by varying only temperature, while holding AH constant.

Because of its simplicity and its ease of implementation, varying the temperature over the 24-hour cycle shown in Table 2 while holding the AH constant at 17.5 g/m^3 is the recommended approach for experimentally reproducing diurnal T and RH cycles.

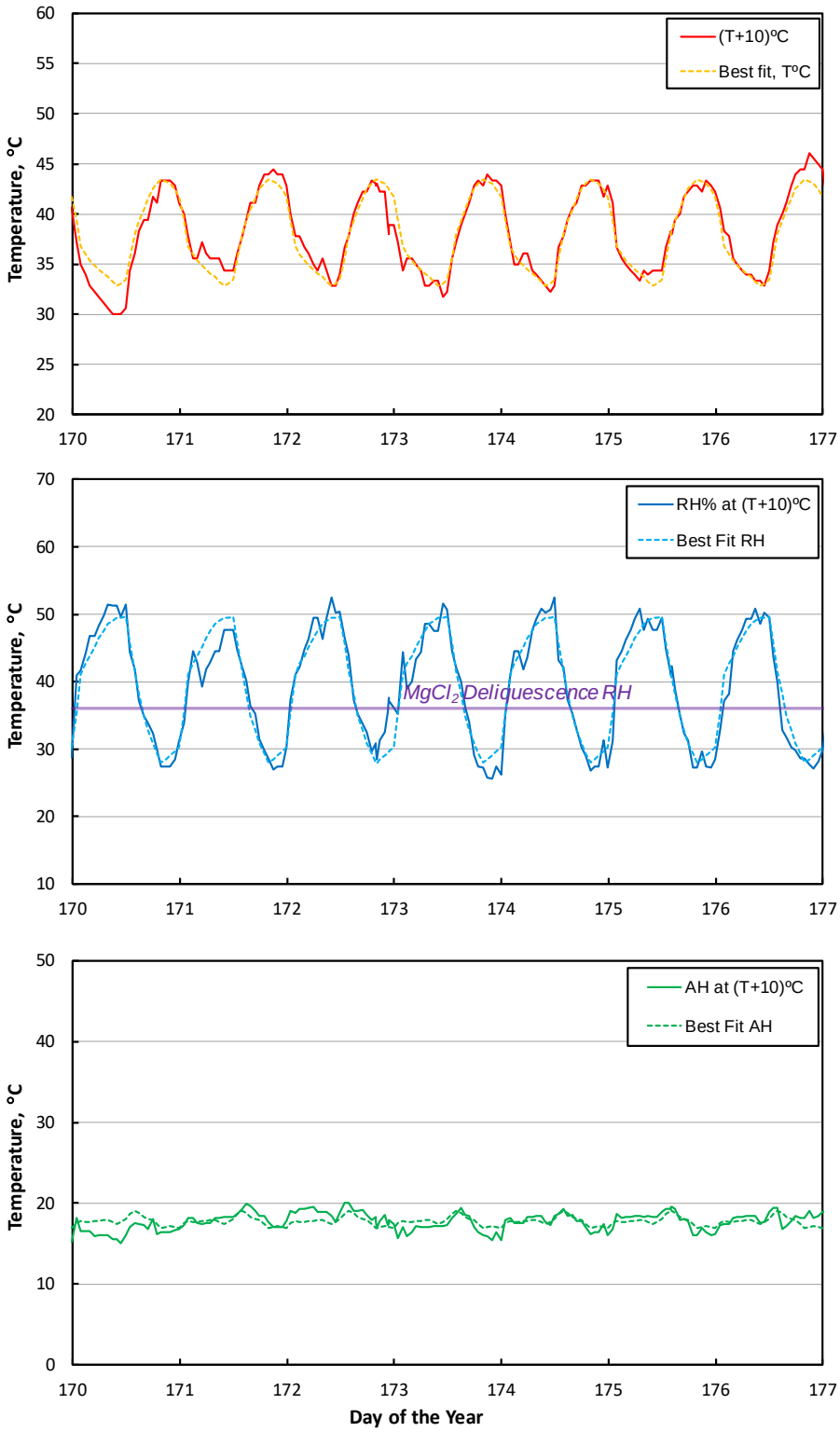

Figure 4. Best fits to the temperature-adjusted weather data, using the 12 step, 24-hour cycle shown in Table 2. Best fit AH values (bottom curve) are calculated from the T and RH fits.

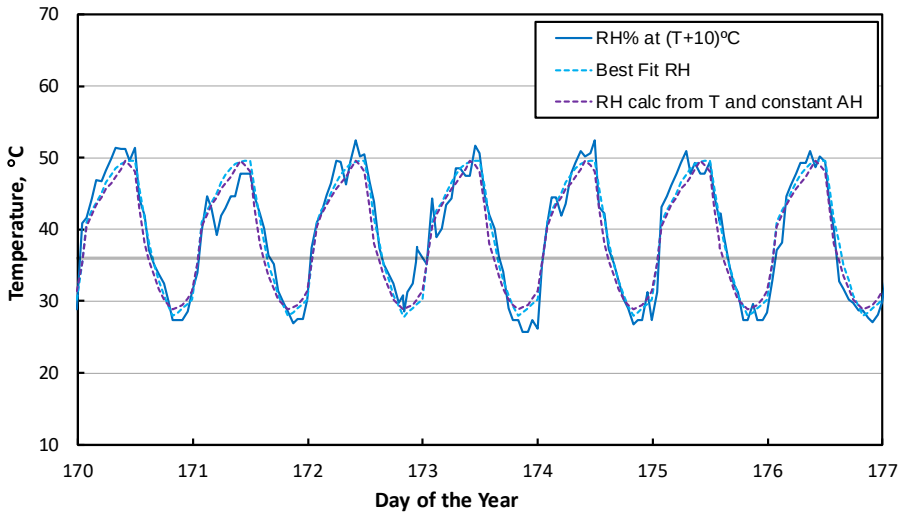

Figure 5. Comparison of temperature-adjusted weather data, the best-fit RH curve (24-hour cycle), and RH values predicted using the best-fit T cycle and a constant AH of 17.5 g/m^3.

2.2 Characteristics of sea-salt brines

Atmospheric aerosol particles have a number of natural sources, such as windblown surface soils/dust, sea spray, volcanic emissions, biosphere emissions, and the condensation of atmospheric gases. In addition, a significant fraction of the modern aerosol loading of the atmosphere results from anthropogenic activities such as fuel combustion. The chemical and physical properties of aerosol particles vary globally. A large fraction of ISFSIs are located in coastal regions, while others are located inland. Typical atmospheric aerosols for the two environments differ. Aerosols in the atmosphere over or near the oceans contain a large proportion of sea-spray-derived salt; sulfates formed by oxidation of sulfide species emitted by marine plankton also contribute to the soluble salt load. The aerosols over continental landmasses generally contain a larger proportion of terrestrial dusts/soil particles, particles derived from reactions of sea salt with atmospheric gases, and particles that have anthropogenic origins (Seinfeld, 1986).

In near-marine settings, chloride-rich sea salts generated by wave action and evaporation of sea-spray can comprise a large fraction of aerosols. The occurrence of sea-salt aerosols on SNF dry storage canisters has been confirmed, when sea-salt aggregates were observed in dust samples collected from canister surfaces at the Diablo Canyon ISFSI (Bryan and Enos, 2014). These salts reflect the composition of sea water, the average composition of which is represented by ASTM simulated seawater (ASTM International, 2008), shown in Table 3. Dominant ions in seawater are Na^+ and Cl^- with lesser amounts of Mg^{2+}, Ca^{2+}, K^+, and SO_4^{2-}. Sea spray evaporates to form salt aerosols, which upon deliquescence form highly concentrated chloride-rich brines (sea salt is approximately 55% Cl by weight).

In FY2017, considerable effort was placed into characterizing the brines that form by deliquescence of sea-salt aerosols, in order to better understand the chemical environment that forms. The chemical and physical characteristics of the brines were either calculated using a thermodynamic speciation and solubility and speciation code, and measured experimentally.

Evaporation is simply the inverse of deliquescence, and the composition of brines formed by deliquescence, as a function of the water activity (a_w) in the brine can be predicted by modeling the evolution of seawater as it evaporates. The compositional evolution of evaporating sea water was modeled using the thermodynamic solubility and speciation modeling program EQ3/6 (Wolery and Jarek,

2003) and the YMP Pitzer database (SNL, 2007). In Figure 6, solute concentrations are plotted against the activity of water in the brine, which is equivalent to the RH in atmosphere in equilibrium with the brine, expressed as a unit value. Inflections in the concentration curves occur when a mineral phase begins to precipitate. In this plot, halite (NaCl) precipitates out at an RH of 74%, and bischofite ($MgCl_2$:$6H_2O$) at an RH of 36%. In Figure 7, the concentrations are given in terms of concentration factor, calculated as (original water mass)/(remaining water mass). In this plot, halite precipitates at a concentration factor of about 11, while bischofite precipitates at a factor of about 222. On the concentration factor plot, solutes plot along straight lines as long as they are conserved in solution (do not precipitate out).

Table 3. Ion Concentrations in Seawater, as Represented by ASTM D1141 Substitute Seawater

Species	µg/mL*
Na^+	11031
K^+	398
Mg^{2+}	1328
Ca^{2+}	419
Cl^-	19835
Br^-	67.8
F^-	1.4
SO_4^{2-}	2766
BO_3^{3-}	25.7
HCO_3^-	146
pH	8.2

* (ASTM International, 2008)

While these plots show the evolution of seawater as it evaporates, deliquescence of sea-salts produces exactly the same fluid compositions at any given RH. At low relative humidities (high degrees of evaporation), predicted deliquescent brine compositions are rich in Mg^{2+} and Cl^-, and somewhat less enriched in Br and B. Other seawater components have been removed by precipitation, and are minor in the remaining brine. Br and B plot as straight lines in Figure 7 because they are predicted to be conserved in solution. However, it should be noted that the YMP database is not qualified for use to predict borate species and contains few borate salts; moreover, the available borate data was limited to 25ºC. For these reasons, the predicted enrichment in B may not be real. Moreover, Br can substitute in limited amounts into chloride minerals, and also is not conserved completely (McCaffrey et al., 1987). Hence, predicted brine compositions at RH values below the deliquescence point of magnesium chloride are speculative.

It is mineral precipitation that ultimately controls the relative proportion of species in the evaporating brine. Salt minerals that are predicted to precipitate out during evaporation are shown in Figure 8. In order of occurrence, calcite ($CaCO_3$) precipitates first, and then gypsum ($CaSO_4$:$2H_2O$), which converts to anhydrite ($CaSO_4$) at a concentration factor of about 9. Halite precipitates at a concentration factor of about 11. Other minerals precipitate, and in many cases re-dissolve, as the seawater evaporates. The final salt assemblage at dryout consists mostly of halite, with minor amounts of bischofite and kieserite ($MgSO_4$:$2H_2O$) and trace amounts of anhydrite, carnallite ($KMgCl_2$:$6H_2O$), and hydromagnesite ($Mg_5(CO_3)_4(OH)_2$:$4H_2O$).

Note that magnesite ($MgCO_3$) is actually predicted to occur instead of hydromagnesite, but has been suppressed in the thermodynamic calculation. This was done because magnesite is kinetically inhibited from nucleating, and is rarely observed to form at temperatures below 100ºC. However, precipitation of $MgCO_3$ has occasionally been achieved at low temperatures, and may be enhanced by cyclic (e.g., diurnal) changes in the environment (Deelman, 1999; dos Anjos et al., 2011). Experimental work described in Section 2.3 may help determine which carbonate actually occurs.

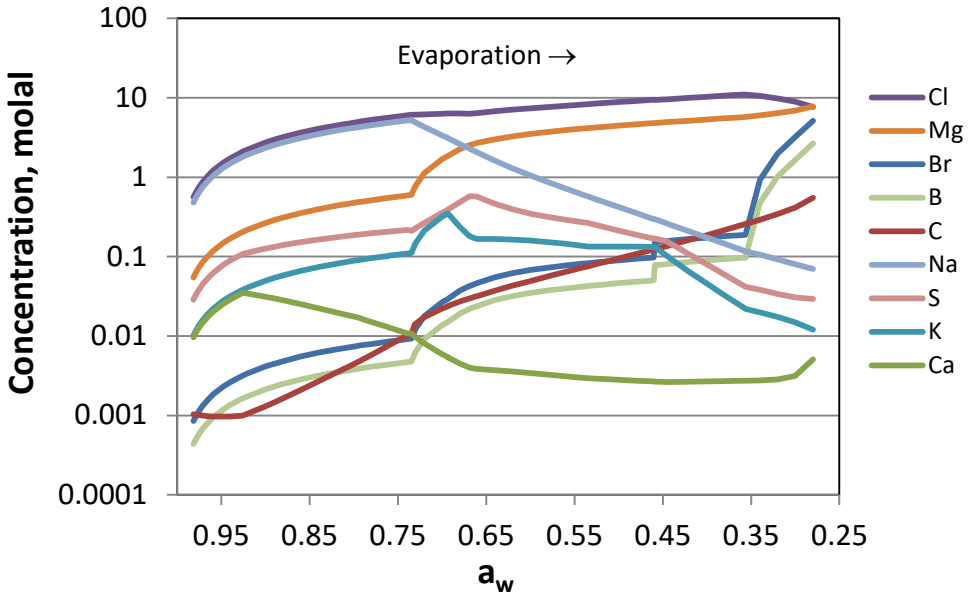

Figure 6. Evaporation of seawater. Predicted brine composition as a function of a_w.

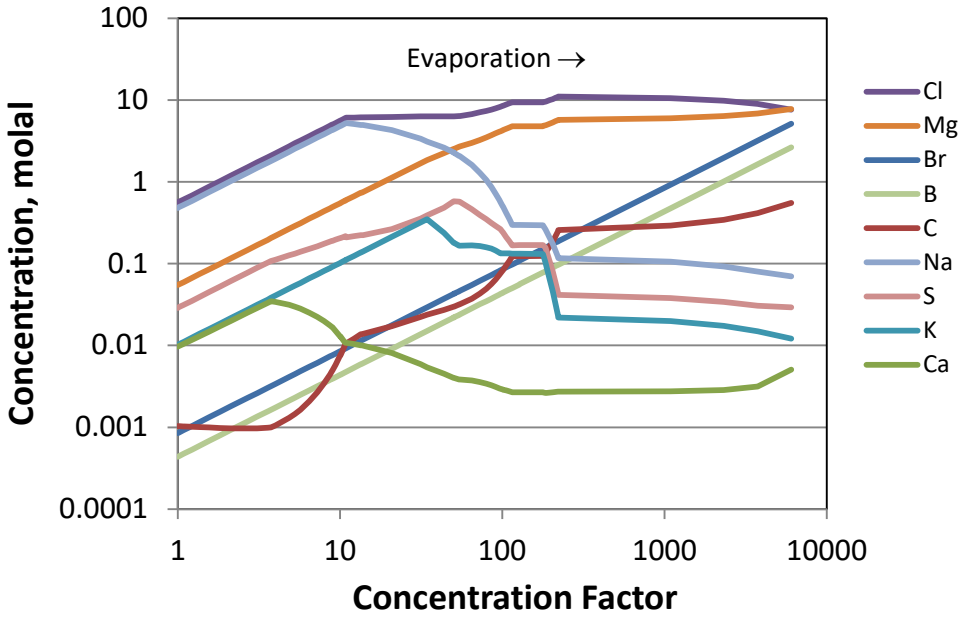

Figure 7. Evaporation of seawater. Predicted brine composition as a function of concentration factor.

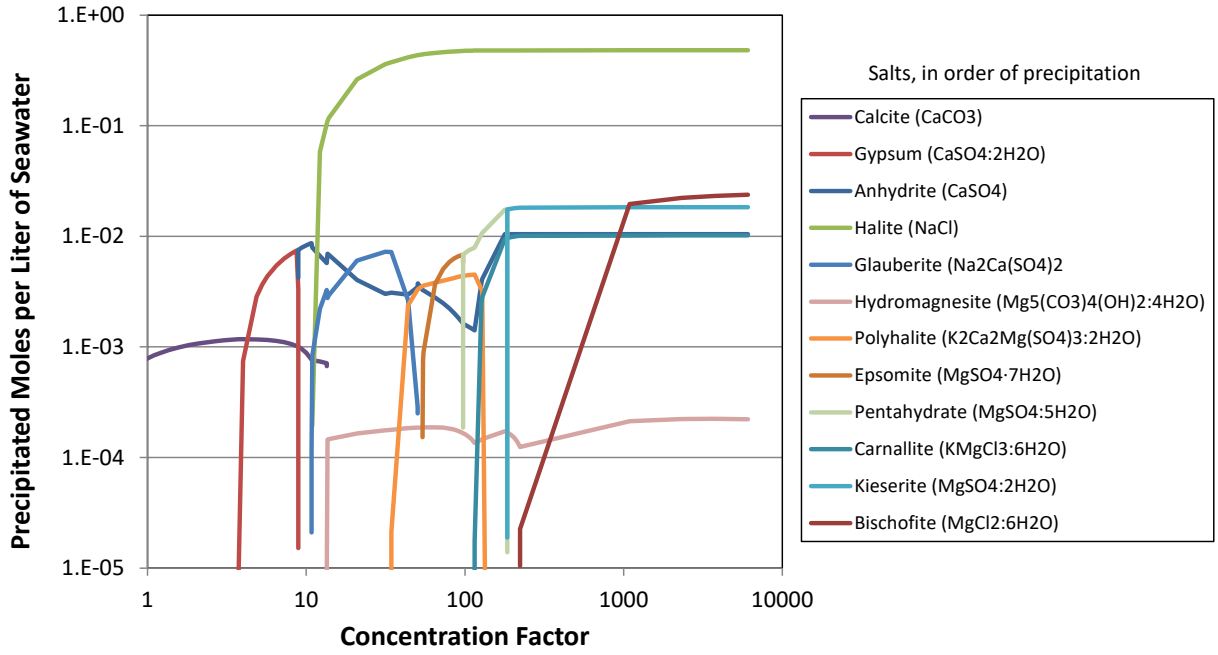

Figure 8. Evaporation of Seawater. Predicted salt phases as a function of concentration factor.

As sea-spray aerosols dry out, the above salts are precipitated. Aerosol particles consisting of salts or a mixture of salts and brine may be deposited on the canister surface, where, at least initially, canister temperatures will be sufficiently hot to completely dry the aerosol particles. As the RH rises over time, the salts re-dissolve and the composition of the deliquescent brine follows the path of evaporation in reverse order. It is the highly deliquescent $MgCl_2$:$6H_2O$ that is believed to control the deliquescence behavior of sea salts; determining when an aqueous phase is present.

The brine compositions predicted here are consistent with thermodynamic modeling by Eugster et al. (1980) and by Harvie et al.(1980), and with experimental studies of seawater evaporation dating back over 100 years, including McCaffrey et al. (1987), and the seminal study by Van't Hoff (1905; 1909; 1912).

The thermodynamic modeling also provides other data that is of important for modeling corrosion processes in relevant brines, and at relevant canister surface temperatures. One parameter of interest is the dissolved oxygen concentration in the brines, as that potentially affects the kinetics of the oxygen reduction reaction (ORR) at the cathode on the metal surface surrounding the corroding pit or crack. Calculated oxygen solubilities in the deliquescent brines, assuming equilibrium with the Earth's atmosphere, are shown in Figure 9 as a function of temperature and equilibrium RH (a_w in the brine). At all temperatures, oxygen solubilities are highest in unevaporated sea-water, and decrease as the water evaporates and concentrates. Above the deliquescence point of NaCl (~74% RH) increasing temperature results in a decrease in oxygen concentration; however, at lower RH values, where sodium precipitates out and the brine becomes progressively more magnesium-rich, the trend is reversed—oxygen concentrations increase with increasing temperature (it should be noted that these trends may in part be due to limitations in the thermodynamic model). If correct, these calculations suggest the following for corrosion under thin films.

- For relatively thick brine films, there should be a compositional dependence to the cathode kinetics. For thick films, oxygen diffusion through the film limits the rate of ORR at the metal surface, and lower solubilities in concentrated brines should slow oxygen diffusion rates.

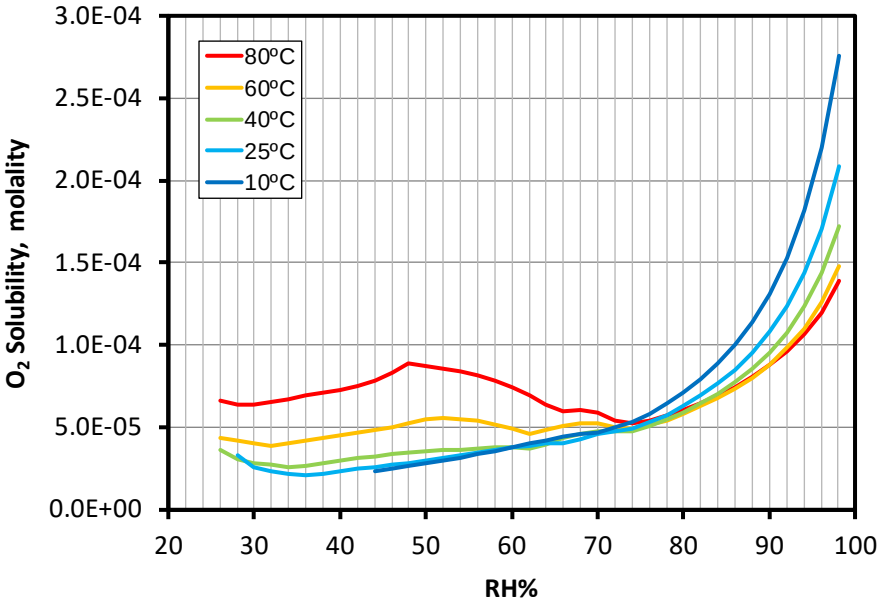

Figure 9. Calculated oxygen solubilities in brines formed by sea-salt deliquescence, as a function of temperature and RH.

- For concentrated brines, lower oxygen solubilities suggest that a thinner brine film is required for oxygen diffusion to cease to be the limiting process for ORR.
- Similarly, at higher temperatures and RH above 74%, a thinner film may be required for oxygen diffusion to cease to be the limiting process. Below that RH, the trend will be reversed. However, higher temperatures also promote more rapid diffusion, which would have the opposite effect.

The cathodic kinetics experiments described in Section 3.3 will allow us to assess the potential effects of brine composition, temperature, and oxygen solubility on the oxygen reduction reaction.

As seawater evaporates, the volume of brine that remains decreases. For a given volume of seawater, equivalent to a given mass of sea-salt aerosol particles, we can use the thermodynamic model to calculate the volume of the brine and of the precipitated salts as a function of RH and of salt surface load. Moreover, if it is assumed that the brine is distributed as a continuous film across the surface, then a brine film thickness can be calculated. As discussed in Section 3.3, this assumption, which requires redistribution of salts on the canister surface, is unproven. However, performing this calculation provides insights into the RH and temperature dependence of the brine volume, and the potential importance of processes dependent upon brine film thickness. The calculation requires brine density as a function of composition and temperature, and these values were measured as a function of temperature for four brines mixed to match compositions along the evolutionary pathway shown in Figure 6, at 98% RH (seawater) 78% RH, 58% RH, and 38% RH (it should be noted that the fact that these brines could be mixed in the exact compositions predicted provides a certain level of validation for the thermodynamic model). Brine densities at intermediate RH values were estimated by interpolation. Through there is some uncertainty in this approach, the effect on predicted brine layer thickness is insignificant.

Figure 10 shows predicted brine layer thicknesses, assuming a continuous film, at 25ºC as a function of RH, for a series of different salt loads. The thickness dependence on RH is the same for all salt loads, as for a given set of conditions (T and RH), brine layer thickness varies linearly with salt load. Inflections in each curve represent RH conditions at which a salt mineral precipitates. In each case, the layer thickness decreases by about a factor of 10 as the RH is reduced from 98% (unevaporated sea-water) to 74%, where NaCl precipitates. The brine thickness decreases an additional order of magnitude as the RH drops to

about 46%, where carnallite precipitates. Below this RH, the brine is nearly pure magnesium chloride. Bischofite precipitates at 36% HR (at 25ºC); as discussed earlier, predicted brine thicknesses below that RH probably reflect limitations of the thermodynamic database with respect to B and Br. An important point is that oxygen diffusion through the brine layer is not anticipated to be limiting with respect to the oxygen reduction reaction at brine films thinner than 20 µm (Nishikata et al., 1997), and calculated brine layer thicknesses below the deliquescence point of NaCl are consistently below this, even for relatively high salt loads. Moreover, the predicted thicknesses are so small that development of a continuous brine film through sea-salt aerosol deliquescence alone seems unlikely.

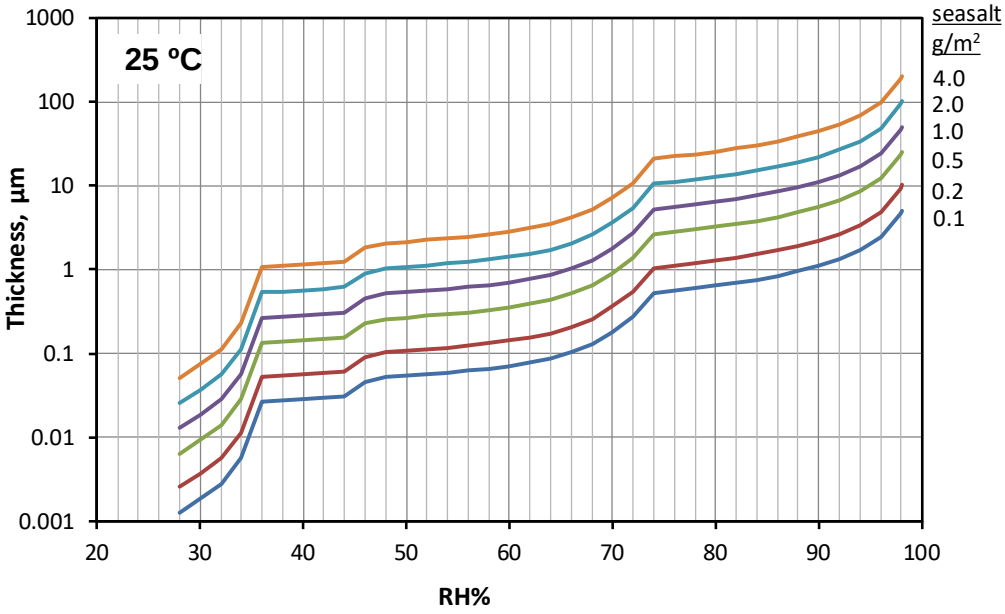

Figure 10. Calculated brine layer thicknesses as a function of salt load and RH.

Calculated brine layer thicknesses as a function of temperature are shown in Figure 11. Temperature has a relatively minor effect on the predicted brine volumes. The identity of the quaternary salt that precipitates at around 45% RH changes with temperature, causing a minor shift in deliquescence RH for that salt. The other change is in the deliquescence point of bischofite, which shifts to lower values with increasing temperature.

Finally, it not obvious, as sea-salts deliquesce dry, how the actual volume of brine present compares to the volume of solid salts present. This information is useful in assessing the degree of continuity in the brine layer that might form by deliquescence of small (generally 10-20 um) sea-salt aerosols. To assess, this, the volume ratio of brine to precipitated solids was calculated as a function of RH. The results are shown in Figure 12. At RH values above the deliquescence point of NaCl, brine volumes are orders of magnitude greater than the precipitated salts, which consist only of small amounts of calcite and gypsum (Figure 8). At RH values below 74%, brine volumes decrease rapidly and precipitated salts increase. By 60%RH, brine/precipitated salt ratios are 2 orders of magnitude lower, with about equal volumes of each. At the deliquescence RH for bischofite, the remaining brine is nearly pure $MgCl_2$, and the ratio of brine-to-solids is about 1/3.

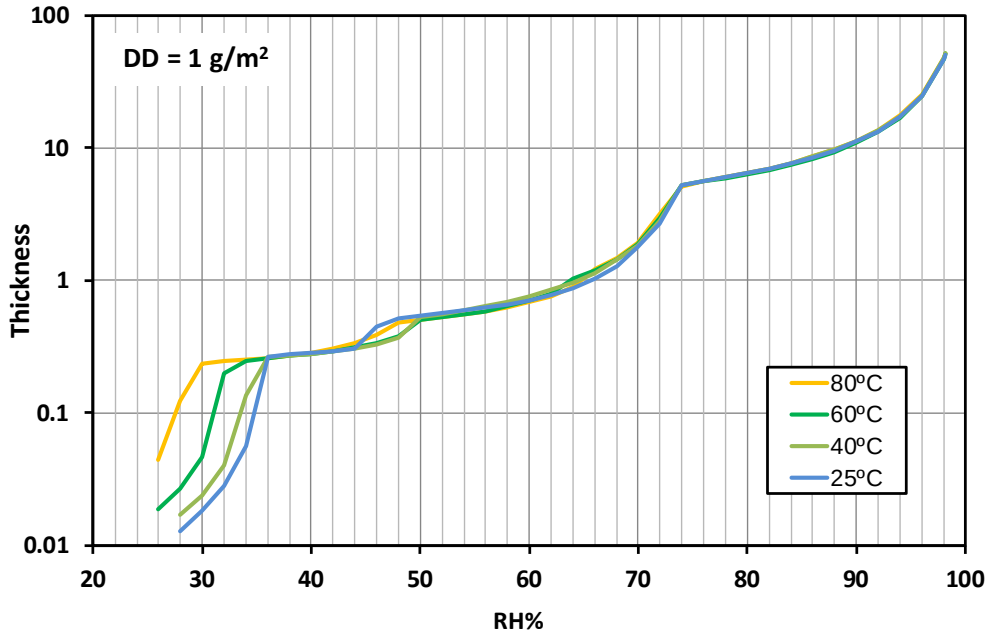

Figure 11. Calculated brine layer thicknesses as a function of temperature and RH.

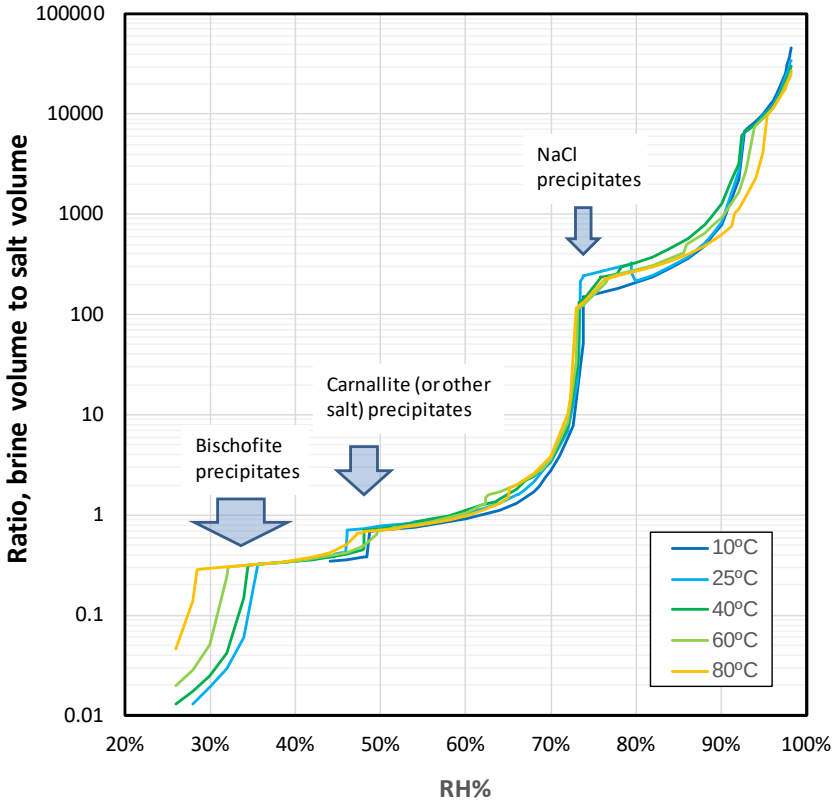

Figure 12. Calculated ratio of brine to precipitated salts, for brines that form by sea-salt deliquescence.

2.3 Experimental evaluation of $MgCl_2$ brine stabilities at elevated temperatures

The thermodynamic calculations in Section 2.2 assume equilibrium with atmospheric CO_2 concentrations, but do not evaluate atmospheric exchange with other atmospheric gases. Several of these are acidification reactions in which acid gases such as HNO_3, H_2SO_4 (or SO_2, which reacts with water to form H_2SO_4), or CO_2 (which forms carbonic acid in solution) are absorbed, and concomitant degassing of HCl occurs. This results in conversion of chloride salts to nitrates, sulfates, or carbonates. Ongoing work is evaluating these effects, both through modeling and experimental studies.

In FY17, we began to evaluate the effects of these reactions on sea-salt brines. Our initial experiments, described here, evaluate potential carbonation of magnesium chloride brine, the brine that would form first as the canister cools and sea-salt aerosols deliquesce. The reaction of interest is:

$$Mg^{+2}(aq) + 2Cl^{-}(aq) + H_2O + CO_2(g) \rightarrow MgCO_3(s) + 2HCl(g)$$

For simplicity, $MgCO_3$ (magnesite) is shown above, but this is just a placeholder. Magnesite itself is kinetically inhibited from precipitating, and a different Mg-carbonate, such as hydromagnesite ($Mg_5(CO_3)_4(OH)_2{:}4H_2O$) is frequently observed experimentally. There are many magnesium carbonate minerals with different CO_3:OH ratios and numbers of waters of hydration, and even a Mg-chloride-carbonate phase is known to exist.

When HCl(g) is degassed, the brine pH rises, causing the HCl(g) partial pressure being generated by the brine to decrease. However, the pH is partially buffered by absorption of CO_2 from the atmosphere and formation of carbonic acid. The carbonate concentration in the brine increases as HCl degassing continues, and the brine eventually saturates with magnesium carbonate, which begins to precipitate out. At this point, the pH is fully buffered, and the brine composition becomes invariant; further degassing continues without affecting the pH or the HCl partial pressure; the brine can fully convert to carbonate. This will occur if the HCl partial pressure being generated at the point of carbonate precipitation exceeds the HCl partial pressure in the environment. As noted in Section 2.2, the brines that are predicted to form by sea-salt deliquescence are in equilibrium with the atmospheric CO_2 levels, and are already saturated with a magnesium carbonate (Figure 8)—HCl degassing has no effect on the brine composition, but results in conversion of $MgCl_2$ to carbonate and dry-out of the brine. As noted previously, magnesite is assumed to be kinetically inhibited, and hydromagnesite precipitates; if magnesite does form, then the pH will be lower at the point of carbonate precipitation, and the HCl partial pressure higher.

To evaluate this thermodynamically, the thermodynamic solubility and speciation modeling program EQ3/6 (Wolery and Jarek, 2003) and the YMP Pitzer database (SNL, 2007) was used. We assume that this reaction can occur as soon as deliquescence occurs (or even before, if a water film forms on the salt surface below the deliquescence RH); therefore Mg^{+2} and Cl^{-} concentrations were fixed to be at saturation with $MgCl_2{:}6H_2O$ (bischofite) at the temperature of interest; this also determines the H_2O activity. The CO_2 gas concentration was set to the current atmospheric value of $10^{-3.4}$ bars. The HCl partial pressure generated by the brine is strongly controlled by the temperature. Therefore, Mg-carbonate and $MgCl_2{:}6H_2O$ (bischofite) stability fields were determined as a function of canister surface temperature and atmospheric HCl(g) concentration. The results are shown in Figure 13; also shown are typical ranges for atmospheric HCl concentrations in marine, continental, and industrial settings (Vierkorn-Rudolph et al., 1984; Möller, 1990; Harris et al., 1992; Kulmala et al., 1998; Crisp et al., 2014).

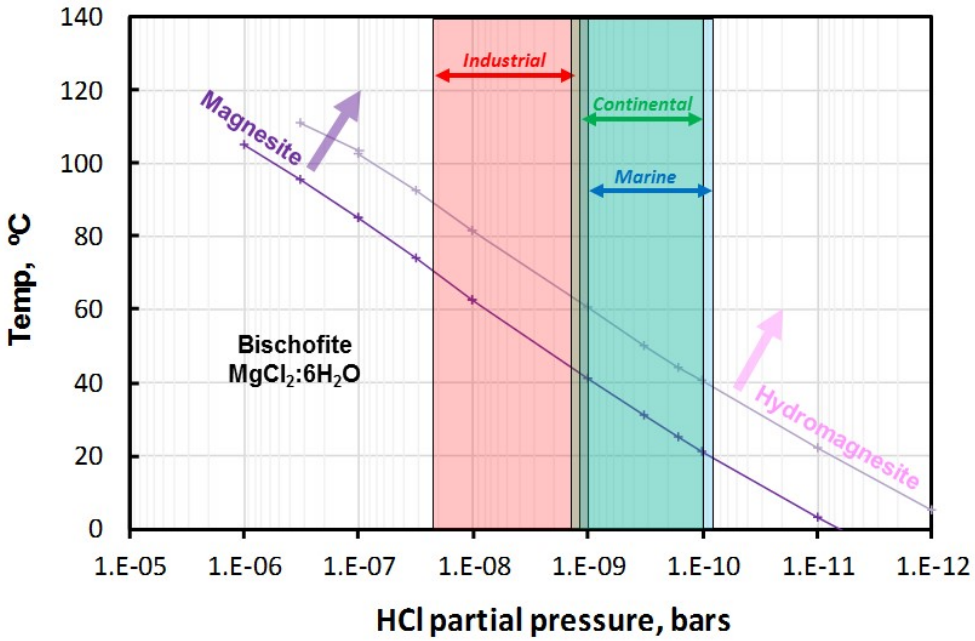

Figure 13. Stability fields for bischofite, magnesite, and hydromagnesite, as a function of temperature and HCl partial pressure.

The modeling indicates that at elevated temperatures, HCl(g) partial pressures generated by the Mg-Cl brine are higher, supporting degassing and formation of Mg-carbonate. Stability fields are shown both for magnesite and for hydromagnesite. As noted previously, magnesite is kinetically inhibited from precipitating in many environments, and the more soluble hydromagnesite actually precipitates. Because hydromagnesite is more soluble, it does not precipitate until the pH has risen to a higher value, corresponding to a higher carbonate concentration in solution and a lower acid gas concentration—that is why the hydromagnesite stability field is shifted to lower HCl(g) values. It is not clear, in concentrated $MgCl_2$ brines with low water activities, if magnesite or hydromagnesite would precipitate. Moreover, there are several other known Mg-carbonate minerals with varying numbers of waters of hydration and varying carbonate to hydroxide ratios, and even a Mg-carbonate-chloride phase; none of these are in the thermodynamic database. At lower temperatures, bischofite is the stable phase over the temperature range of interest.

It is important to note, also, that the HCl partial pressures that are generated by the brine as it degasses on the phase boundary are very low at relevant temperatures. For instance, if magnesite is the solubility limiting carbonate, then at 60ºC, the HCl partial pressure would be only about 1×10^{-8} bars, corresponding to only about 14 µg/m^3. If hydromagnesite is the precipitating phase, then the HCl partial pressure is an order of magnitude lower, corresponding to 1.3 µg/m^3. These low capacities for chloride removal may limit the extent of degassing in laboratory settings where air flow rates are low; however, estimated air flow rates through interim storage canister overpacks are on the order of cubic meters per minute, and degassing should not be constrained by limited air volumes. However, the efficiency of HCl loss from the brine surface is also not known, and may be kinetically limiting.

Given the incomplete thermodynamic data and the potential for kinetic limitations on degassing, the occurrence and rate of this reaction was evaluated experimentally. To do this, magnesium chloride brine (1M, in 17% ethanol solution) was sprayed onto an inert substrate—polished silicon wafers 25 mm in diameter—using an ink-jet printer as described in Schindelholz and Kelly (2010). This deposition method produced randomly-spaced, isolated droplets of brine on the wafer surface, 10 to 30 microns in diameter. Using dispersed droplets greatly increases the brine surface area-to-volume ratio, and increases

the rate of exchange with the gas phase. This is realistic—the droplets are only slightly larger than sea-salt aggregates collected from in-use storage canisters at the Diablo Canyon ISFSI (Bryan and Enos, 2014), which were ~10 µm in diameter. The initial salt load was about 88 µg/sample $MgCl_2$ (17.4 µg/cm^2), or 65.6 µg/sample Cl (13 µg/cm^2).

After salt deposition, the wafers were stored in a nitrogen purged cabinet until use. Three samples were retained to quantify the initial condition, and the remaining six samples were placed in a controlled-humidity chamber at 48º C and 40% RH, slightly above the deliquescence RH of $MgCl_2$:$6H_2O$ 35% at that temperature). The atmosphere in the chamber was replaced at a rate of 2 L/min, using air that had been passed through a "Zero Air" system capable of removing all contaminants (organic compounds and acid gases) from the air stream. CO_2 was not removed by the Zero-Air system. Three samples pulled after 30 days, and the final three, along with a blank wafer as a control, after 69 days. All samples were stored in a cabinet purged with dry nitrogen until analysis.

In order to determine if partial or complete conversion to carbonate occurred, the samples were analyzed in several ways. First two samples, one unexposed and one exposed for 68 days, were retained for analysis by Time-of-Flight Secondary Ion Mass Spectrometry (TOF-SIMS). These samples have not yet been examined. Then, one of the 68-day samples was analyzed by Scanning Electron Microscopy (SEM) and Energy Dispersive X-ray Spectroscopy (EDS). Finally, with the exception of the samples still awaiting TOF-SIMS analysis, all samples were leached with deionized water, and the dissolved salts were analyzed by ion chromatography (IC). This does not provide information on carbonate, but does give Mg and Cl concentrations.

2.3.1 SEM/EDS analysis

For SEM EDS analysis, the 68-day sample (#16) was coated with a ~10 um thick coating of Au/Pd to make it conductive for improved imaging and EDS analysis. Imaging, analysis, and element mapping was done with a Tescan Vega3 SEM, equipped with an EDAX Element® EDS detector. An accelerating voltage of 15 keV was used, and working distances of 9 to 12 mm, with varying degrees of magnification. Images were obtained using secondary electron (SE) imaging and a beam current of 100-150 pA. A higher beam current of 400-800 pA was used to produce a high count rate for EDS analysis and element mapping.

A low magnification image of Sample #16 is shown in Figure 14. The image shows the distribution of the brine on the silicon wafer, occurring as randomly located, but non-overlapping droplets. Varying in size from 10-30 um in diameter. Originally present as liquid droplets in the humidity chamber, the droplets are dried in the vacuum of the SEM, and occur in different morphologies. The most abundant, comprising 80-90% of the total, are droplets that dried to leave a smooth but wrinkled, "raisin-like" surface. 10-20% of the droplets dry to form rings, with elevated edges and smooth centers. Finally, rare droplets dried to form rough-surfaced particles, leaving a residue behind as they evaporated and shrank towards the center of the original drop.

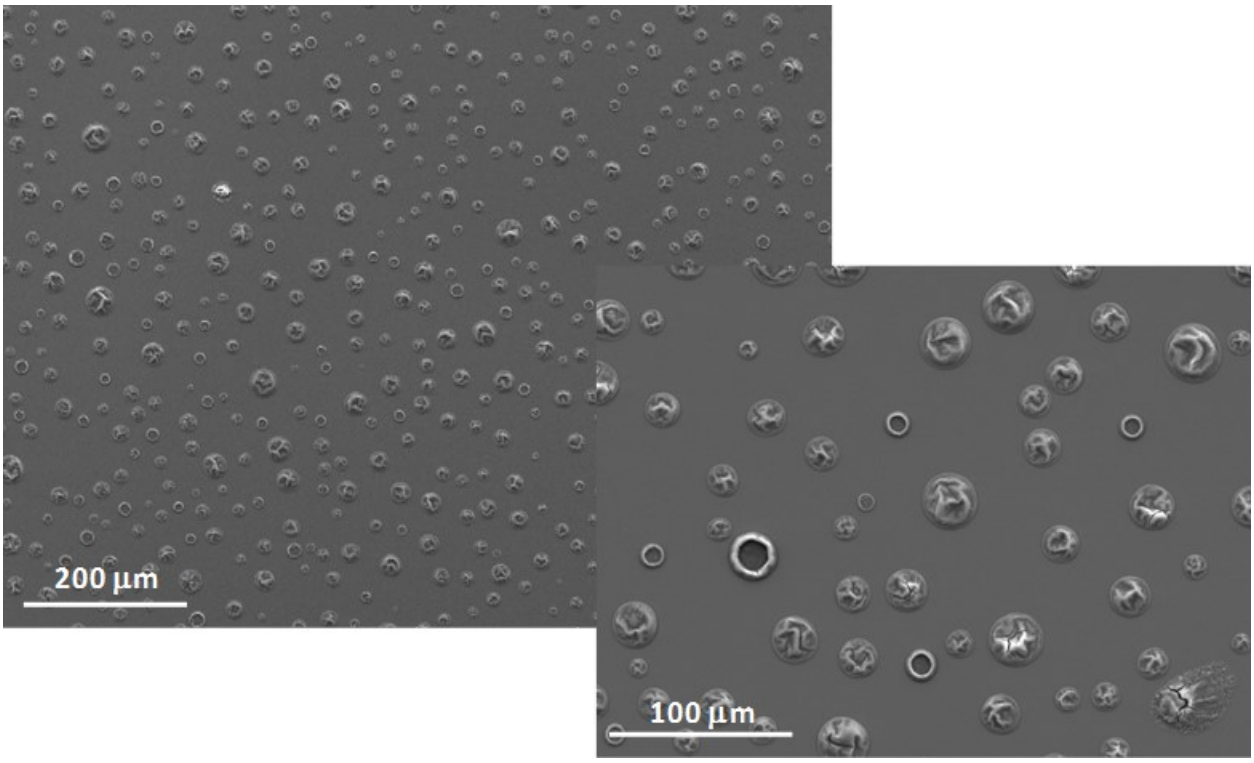

Figure 14. SE images of Sample #16, exposed for 68 days, illustrating the two different droplet morphologies.

Element maps of a region including several droplets are shown in Figure 15, and it is immediately obvious that there is a strong compositional control on droplet morphology; the ring-like droplets contain carbon, while the more abundant wrinkled droplets do not. A highly magnified image of a pair of droplets is shown in Figure 16, with element maps and EDS X-ray spectra, illustrating the difference in composition. The carbon peak is small, but distinct, in the ring droplet. Additional images and X-ray spectra are shown in Figure 17, confirming the relationship between composition and droplet morphology. Note that the ring droplets also contain carbon in the flat cores; the carbon peaks are lower than in the rims, but the peaks for Mg, Cl, and O are also lower. The differences in peak heights between the cores and the rims are likely due to differences in salt thickness and the overall volume of salt excited by the electron beam, as opposed to actual differences in composition between core and rim.

The differences in chemistry between the salt grains are responsible for the differences in morphology. The wrinkled, carbon-free grains are bischofite, Mg_6Cl_2:$6H_2O$ displaying large peaks for Mg, Cl, and O. The wrinkled surface is probably a gel-like cap that formed upon drying, trapping brine underneath, a commonly observed feature of magnesium chloride brines (Schindelholz et al., 2013). The carbonate-containing grains have partially converted to Mg-carbonate, still showing large chloride peaks. Magnesium carbonates are much less deliquescent than magnesium chloride and the carbonate would not be deliquesced at 40% RH. Hence, as the conversion progressed, the volume of brine in the droplet decreased, resulting in the formation of a flatter droplet upon drying of the brine. Moreover, the conversion to carbonate results in a large mass and volume loss in the dried salts, because the carbonates do not contain as much water as the bischofite.

It is notable in that only the ring-like droplets show evidence of reaction; there is no carbon in the wrinkled droplets. Apparently, not all droplets reacted; each droplet either degassed HCl and absorbed CO_2, or it didn't react at all. It is not clear why this would occur, but there appears to be some

relationship to droplet size. The ring-shaped droplets are in the mid-to-small size range (Figure 14 to Figure 17). The largest droplets are never of the ring variety, but only a fraction of the mid-to-small droplets reacted. We speculate that surface tension effects associated with the higher radius of curvature for the smaller droplets results in a greater tendency to react, possibly by resulting in more concentrated brine and generating higher vapor pressures of HCl. However, why only some droplets would be affected is not clear. Further characterization by TOF-SIMS and by Raman Spectroscopy is planned, and may shed some light on the actual conversion reaction that occurs.

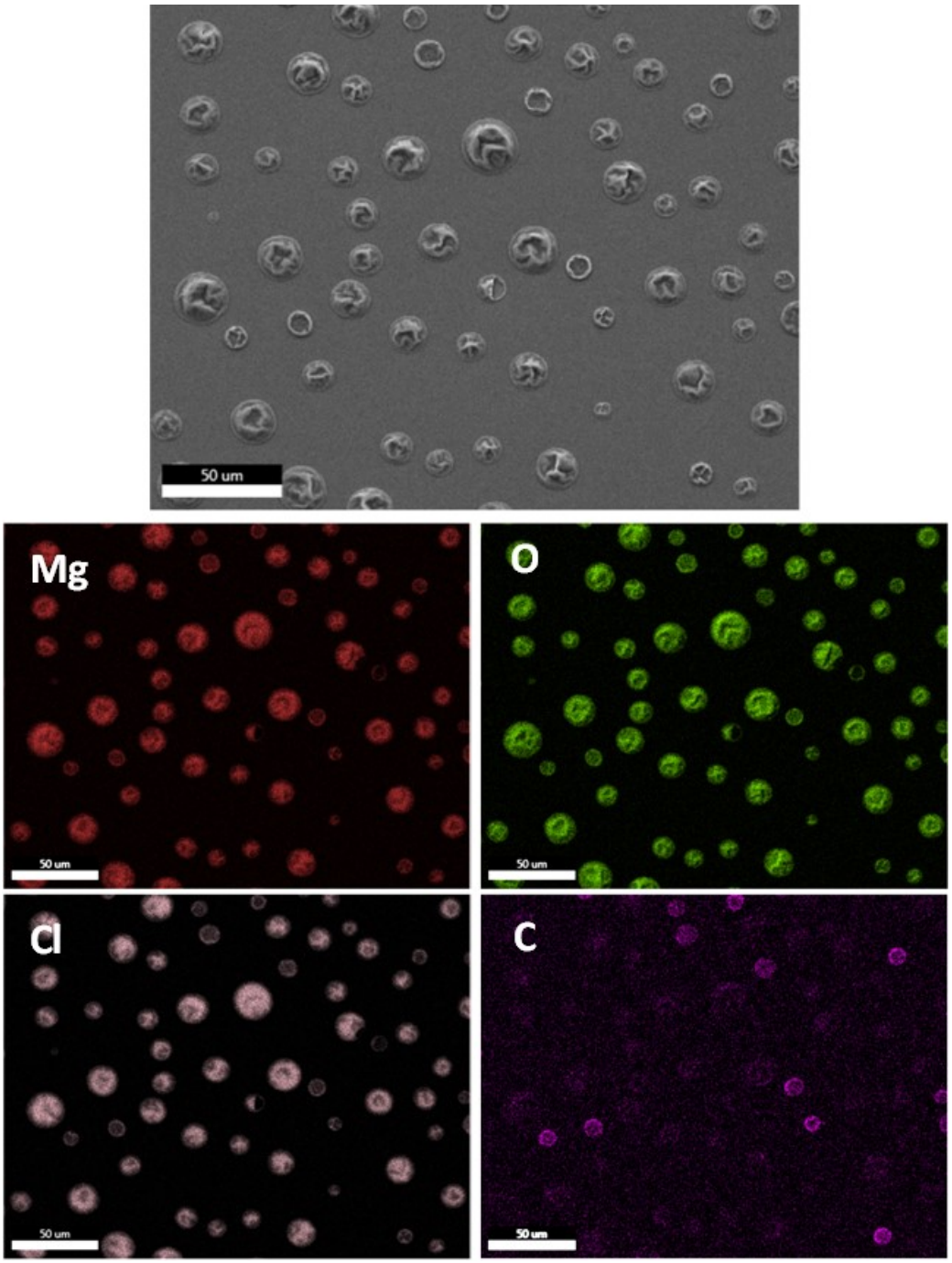

Figure 15. Element map of dried salt droplets on Sample #16, exposed for 68 days illustrating the relationship between morphology and composition.

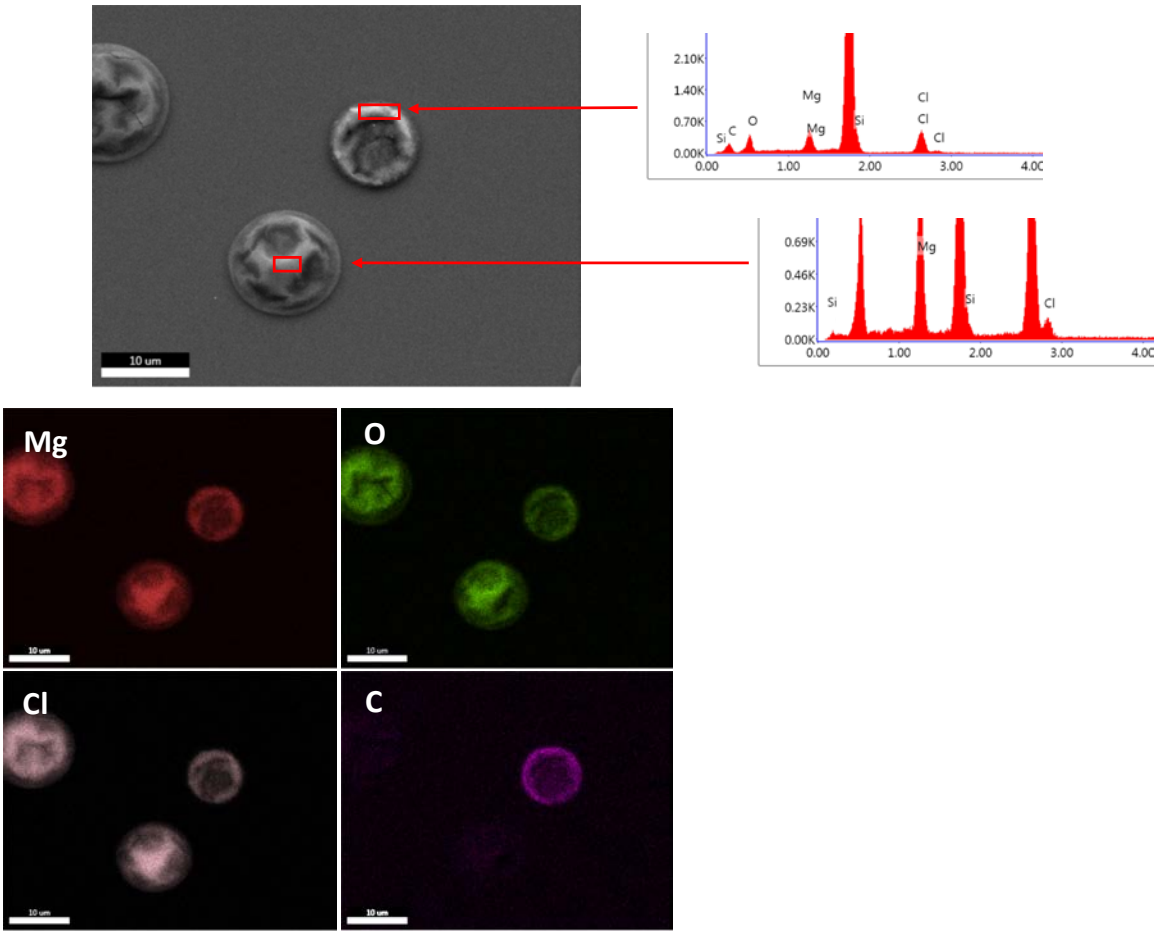

Figure 16. Magnified SE image of two droplets on Sample #16, with element map and X-ray spectra. Only the ring-like droplet contains carbon.

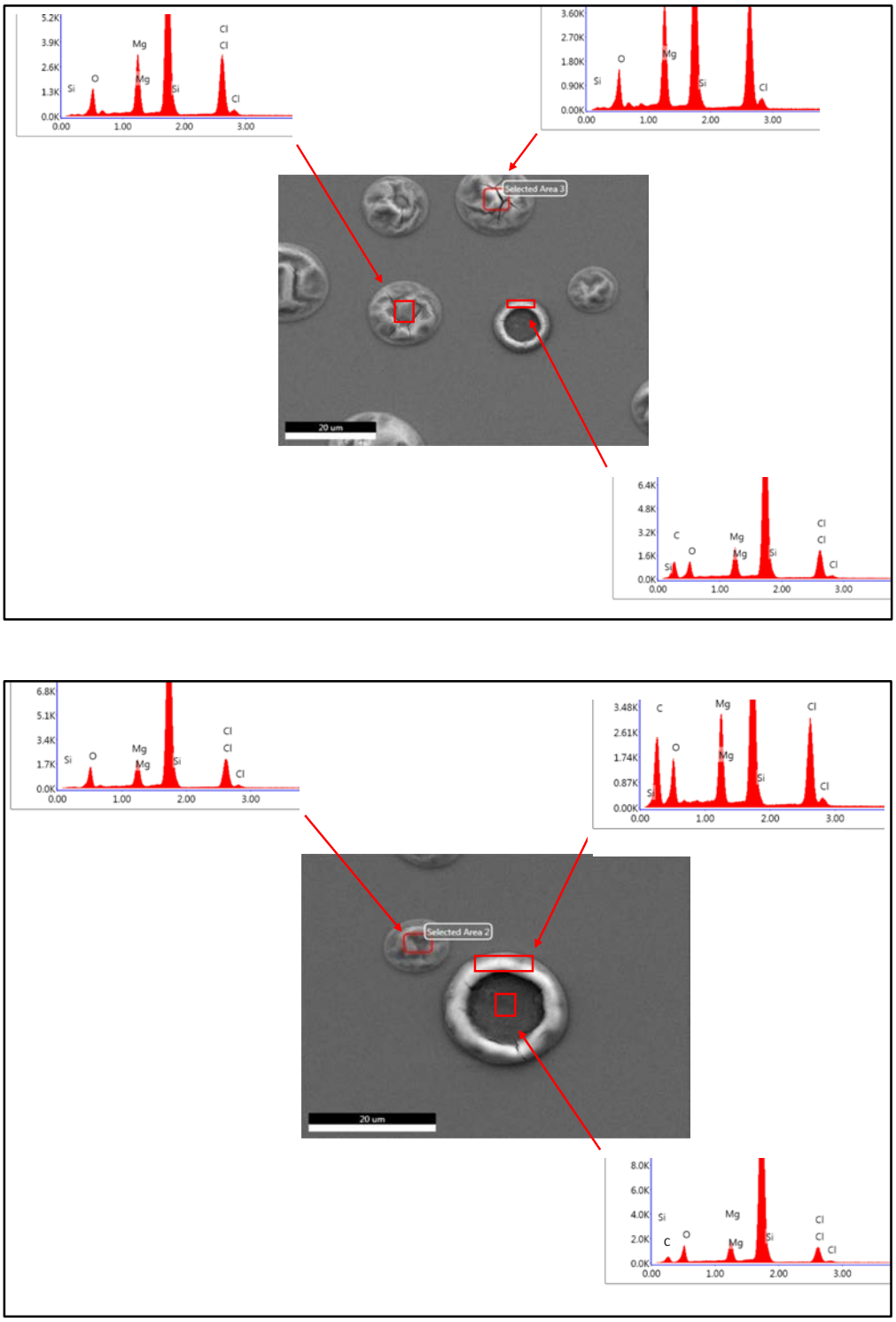

Figure 17. SE images and X-ray spectra for dried magnesium chloride droplets, illustrating the compositional dependence of droplet morphology.

2.3.2 Chemical analysis of salts leached from the sample wafers

In order to quantify the extent of reaction, the salts were leached form the wafers and analyzed by IC. First, the silicon wafers were transferred to sterile 50 ml polypropylene tubes, and 20 ml of deionized water was added. The tubes were gently agitated for one hour to leach off the salts. Then, 5 ml aliquots were extracted and added to sample vials for IC analysis. Anionic analytes were F^-, Cl^-, Br^-, NO_2^-, NO_3^-, SO_4^{-2}, and PO_4^{-3}; however, Br^- and NO_2^- were never detected, and are not included here. Anion IC analyses were done with a Dionex ICS-1100 RFIC Ion chromatograph with a Dionex Ionpac AS-23 RFIC column and AG-23 guard column, and a Dionex AERS 500 suppressor. Cationic analytes were Li^+, Na^+, NH_4^+, K^+, Mg^{2+}, and Ca^{2+}, and were run using with a Dionex Ionpac CS-12A column and CG-12A guard column, and a CERS 500 suppressor, all 4 mm in diameter. In both cases, blanks were run after every sample to minimize carryover, but little was observed. Calibration standards were made by dilution of stock Dionex IC anion and cation standards. Sample concentrations were estimated using a subset of the standards (never less than three and a blank), excluding those which were higher than necessary to constrain the sample concentration. This was done because the calibration curves were based on the least squares method, which over-weights higher-concentration standards and results in larger errors for values in the lower part of the range. All standards and eluents were purchased for this analysis, and were well within their expiration dates.

Results of the chemical analyses are shown in Table 4. Values in black text are accurate to ±3% (analytical uncertainty), based on the results of standards run as unknowns. Italicized grey values are indications only, species that showed up as distinct peaks not present in the blanks, but at concentrations below the lowest standard used—too low to quantify accurately. In the samples, only Mg and Cl were detected in significant amounts. Na, K, and F consistently showed up in the samples at very low concentrations, below the limit of quantification; they were not present in the blanks. Ca and SO_4 were not detected in any sample or blank. Small amounts of ammonium and chloride were detected on the control sample, but ammonium was not detected in any other sample.

Results for species that were present in quantifiable amounts are shown in µEq/sample (µEq = moles × ion charge) in Table 5. Upon deposition as $MgCl_2$ brine, the Mg^{2+} and Cl^- concentration in µEq would have been equal. HCl degassing would have resulted in loss of chloride, but would not affect Mg concentrations. Hence, the difference between the Mg^{2+} concentration and the Cl^- concentration in µEq is the amount of chloride that was lost by degassing. The percent of the initially deposited chloride that was lost by degassing is shown in Table 5, and is plotted as a function of equilibration time in Figure 18. Although the data are scattered, there is a strong trend of increasing chloride loss with exposure time, indicating that degassing occurred (analysis of the additional two samples at 0 and 69 days after TOF-SIMS analysis may provide increased confidence).

The degassing process was slow; for the two samples analyzed after 69 days, the percent converted was 13.6% and 21.5%. Only partial conversion was anticipated, however. At the HCl partial pressures predicted by the thermodynamic calculations (Figure 9) each cubic meter of air passing through the humidity chamber could only remove ~0.4 µg (hydromagnesite-buffered) to ~3 µg (magnesite-buffered) of chloride, assuming complete equilibration between brine and atmosphere. At the gas flow rate used (2 L/min) and the measured salt loadings (65.6 —g/sample), a single sample would take 15 days (magnesite) to 112 days (hydromagnesite) to fully degas. With six samples in the chamber for the first 30 days and three samples for the next 38 days, full degassing was not possible, even if complete equilibration between the headspace gas and the deposited samples had occurred. While complete degassing was not possible in this experiment, no such limitation is present for magnesium chloride on a canister surface, because airflow through overpacks is on the order of cubic meters per minute, based on computational fluid dynamics calculations of heat-driven advection through the systems (Suffield et al., 2012).

Table 4. Measured ion concentrations (µg/sample)

Sample #	Equilibration Time, days	Concentration, µg/sample							
		Na^+	NH_4^+	K^+	Mg^{2+}	Ca^{2+}	F^-	Cl^-	SO_4^{2-}
MgCl2-11	30.0	*0.2*	—	*0.3*	22.1	—	*0.2*	58.2	—
MgCl2-12	0.0	Sample retained for TOF-SIMS analysis							
MgCl2-13	30.0	*0.3*	—	*0.2*	22.3	—	*0.6*	59.2	—
MgCl2-14	68.9	*0.2*	—	*0.2*	23.1	—	*0.3*	58.3	—
MgCl2-15	0.0	*0.4*	—	*0.2*	23.4	—	—	62.6	—
MgCl2-16	68.9	*1.2*	—	*0.3*	22.6	—	*0.5*	51.8	—
MgCl2-17	0.0	*0.3*	—	*0.4*	21.0	—	—	64.3	—
MgCl2-18	30.0	*0.3*	—	*0.3*	22.9	—	*0.2*	62.8	—
MgCl2-19	68.9	Sample retained for TOF-SIMS analysis							
MgCl2-20 (control)	68.9	*0.2*	3.5	*0.4*	—	—	—	8.0	—

Table 5. Measured ion concentrations in µEq, and % Cl lost by degassing,

Sample #	Equilibration Time, days	Concentration, µEq/sample			% Cl lost
		NH_4^+	Mg^{2+}	Cl^-	
MgCl2-11	30.0	—	1.82	1.64	9.9
MgCl2-12	0.0	Sample retained for TOF-SIMS analysis			
MgCl2-13	30.0	—	1.83	1.67	8.9
MgCl2-14	68.9	—	1.90	1.64	13.6
MgCl2-15	0.0	—	1.93	1.77	8.4
MgCl2-16	68.9	—	1.86	1.46	21.5
MgCl2-17	0.0	—	1.73	1.81	-4.9
MgCl2-18	30.0	—	1.88	1.77	5.9
MgCl2-19	68.9	Sample retained for TOF-SIMS analysis			
MgCl2-20 (control)	68.9	0.19	—	0.23	—

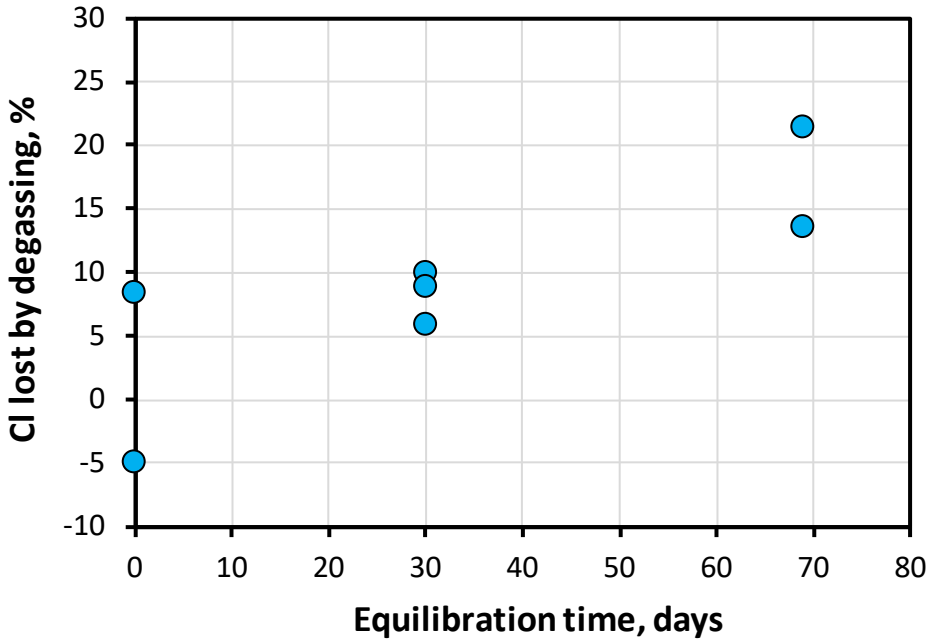

Figure 18. Fraction of Chloride Lost, as a Function of Equilibration Time.

2.3.3 Discussion

This experiment demonstrates that $MgCl_2$ brine at elevated temperatures can degas HCl while absorbing CO_2 from the atmosphere, converting to non-deliquescent magnesium chloride. The experiment was specifically designed to promote degassing; HCl and other acid gas concentrations in the air stream were held at zero. The range of naturally occurring atmospheric HCl concentrations in marine, continental, and industrial areas is shown in Figure 13. Under natural conditions, carbonation can occur in the part of each range that is above the phase boundary, so long as the magnesium chloride is deliquesced, or at least has adsorbed water films. As discussed previously, this corresponds to temperatures up to perhaps 70°C. In the marine and continental ranges, a significant fraction of the range is below 70°C but above the phase boundary, indicating that conversion to carbonate could occur. In industrial areas, high HCl partial pressures may inhibit carbonation. It is also important to note that, in this simplified system, as temperatures drop, the reaction will occur in reverse—the magnesium carbonate will absorb HCl and form a magnesium chloride brine again.

However, under natural conditions other reactions can occur. Absorption of CO_2 is an acidification reaction, resulting in the formation of carbonic acid. Much more effective acidification reactions commonly occur, in which acid gases such as HNO_3, H_2SO_4 (or SO_2, which reacts with water to form H_2SO_4) are absorbed, and concomitant degassing of HCl occurs. This results in conversion of chloride salts to nitrates or sulfates. All of these reactions may occur, depending upon the partial pressures of the acids in the surrounding atmosphere. Future experiments will evaluate these other reactions under relevant acid gas partial pressures.

However, the carbonation reaction described here may be critically important when considering experimental systems. Corrosion experiments are frequently carried out for very long time periods (many months or even years), and the total amount of $MgCl_2$ present within the RH chamber may be small. Moreover, concentrations of other acid gases in laboratory settings may be low, and, if experiments are run under “accelerated” conditions, the possible temperatures may higher. For example, SCC crack growth experiments carried out by the Japanese Central Research Institute of the Electric Power Industry

(CRIEPI) were run at 80°C and 35% RH (conditions not possible in nature). At that temperature, the HCl partial pressure generated by the brine is 30 times higher than in the experiment described here. Moreover, the total amount of $MgCl_2$ present on the CRIEPI samples was small – the salt load was 20 µL of seawater deposited on 3 samples (only a tiny fraction of that will be present as $MgCl_2$ brine at 35% RH), and 20 µL of $MgCl_2$ brine on the fourth sample. The experiments were run for 4000-8000 hrs. Depending upon air flow rates through the humidity chamber and acid partial pressures in the incoming air, complete conversion of the $MgCl_2$ to carbonate could certainly occur, especially on the samples that were treated with seawater, which had orders of magnitude less $MgCl_2$ brine than the sample treated with pure $MgCl_2$. The crack growth rates on the samples treated with seawater greatly slowed after a few thousand hours, but the growth rate for the $MgCl_2$-treated sample did not slow. We speculate that the brine on the seawater samples may have simply dried out due to the carbonation reaction described here.

Under SNF storage canister surface conditions, the carbonation reaction examined here may be of secondary importance relative to other acidification reactions. However, it may be critically important to planning and interpreting laboratory corrosion experiments. As with the CRIEPI experiments, experiments may be carried out for years within controlled-atmosphere chambers. The stability of the corrosive chloride-rich brines that form in such chambers will be completely dependent on acid gas concentrations in the laboratory air entering the RH chamber (HCl, HNO_3, H_2SO_4, and CO_2). These gases are never measured or even considered, but may greatly affect experimental results, especially if the number of samples in the RH chamber is small and the salt load is light (limiting the amount of chloride present); or the experiment is run under ‘accelerated” (high temperature) conditions. This experiment highlights the importance of a mechanistic understanding of the environment in which corrosion occurs.

This page is intentionally left blank

3. RELATIONSHIP BETWEEN CORROSION DAMAGE AND SURFACE ENVIRONMENT

There are presently no models that can effectively describe the population of pits that exist at a particular time on an interim storage canister surface. Application of existing probabilistic and deterministic pitting and SCC models, or development of new models, requires (1) an improved understanding of how surface environment relates to damage evolution in canister-relevant conditions, and (2) datasets that relate extent of damage to measureable surface environment parameters (e.g. RH, T, salt load). Information in both areas is lacking in the literature with respect to canister-relevant conditions. This thrust aims to experimentally define the relationship between environment and corrosion damage kinetics and distributions (e.g. pit size and shape) in simulated near-marine environments. Furthermore, we aim to understand factors controlling the transition from pits to stress corrosion cracks.

3.1 Pitting Kinetics and Damage Distributions

In the second quarter of FY17, we initiated the first of a series of experiments to quantify damage that evolves on austenitic stainless steels exposed to ISFSI-relevant fixed humidity and temperature conditions. These experiments will be specifically utilized to develop datasets on pit frequency and size distributions as function of time and environment. This data will be utilized to inform and benchmark statistical and deterministic SCC models under development at SNL, OSU and CSM.

The experiments consist of exposing 304L, 304H (sensitized and unsensitized) and 316L coupons loaded with artificial sea salts at fixed relative humidity and temperature for up to two years. Sets of coupons are removed from the exposure chamber periodically, the corrosion products removed using standard descaling techniques, and the damage quantified using optical profilometry. This work is being carried out in collaboration with Prof. Jennifer Locke at Ohio State University.

The environmental conditions of interest and relevant to expected canister conditions are shown in Table 6; at absolute humidities that occur naturally, the greyed-out combinations of temperature and RH are not achievable. The remaining conditions represent the range of environments at which deliquesced brine could occur on the canister surface. Highlighted in green are the two conditions currently under test. These represent two humidity conditions where we would expect pitting to potentially be severe. 40% RH is just above the deliquescence RH for magnesium chloride at this temperature, results in a highly concentrated but small volume of magnesium-chloride rich brine, while 75% RH is just above the deliquescence point for sodium chloride in sea-water, resulting in a much larger volume of still-concentrated (~6 M) brine. Over 300 coupons loaded with 10 and 300 $\mu g/cm^2$ of artificial sea salt, deposited as artificial sea-water (ASTM International, 2008) and evaporated, are being exposed to these conditions. These loads represent a lower and higher value within the range reportedly measured on canisters or surrogate surfaces in marine conditions (EPRI, 2015).

Two surface finishes are being examined, a mirror finish and a 120 grit “mill” finish. The latter was chosen as representative of the as-built canister surfaces. Surface finish is expected to have considerable impact on pitting kinetics and size distributions (Burstein and Pistorius, 1995; Moayed et al., 2003). Rougher surfaces are generally more prone to pit initiation, which has been attributed to occluded regions in the ground surface and, possibly, localized residual stress/strain that can act as pit initiators. The mirror surface was chosen as it provides uniform background for analysis of the surface chemistry that develops as a result of corrosion, as will be discussed in Section 3.3.

Table 6. Experimental Matrix for Initial Pitting Corrosion Experiments.

%RH	Temperature (°C)				
75	35				
70	35				
65	35				
60	35				
55	35	40			
50	35	40			
45	35	40	45		
40	35	40	45		
35	35	40	45	50	
30	35	40	45	50	

The experimental approach emphasizes a novel, high-throughput sample preparation and analysis methodology to address the large parameter space under exploration and need for statistically relevant datasets. An inkjet printing technique is utilized for rapid and rigorously controlled deposition of simulated seawater (ASTM International, 2008) droplets on the sample surfaces (see, for instance, Figure 14). Using this unique capability, we can prepare hundreds of samples per day. Corrosion damage morphology (e.g. pitting) is analyzed using a white light interferometer at OSU to create 3D profiles of the exposed coupons. A profilometer is in the process of being purchased at SNL, and future analyses will in part be done at SNL. The profiles are analyzed using a commercial software package capable of automatic detection and measuring individual pit features. Combined, these capabilities enable us to develop datasets necessary for model development.

Initial results of damage morphology and pit statistics for a single sample after one week of exposure are exemplified in Figure 19. Note that pit sizes are on the order of surface roughness and there may be some error here with regard to misidentification of pit-like surface roughness features as actual corrosion pits. To minimize this error, pits identified in the profiles were compared to optical images of the same features to verify the presence of corrosion, and the identification of the features as corrosion pits. Average pit size is anticipated to become larger (potentially to hundreds of microns) with increased exposure time. Additional statistics we are collecting are maximum pit diameter, average depth, volume and principle curvature. The latter descriptor could be utilized to determine the probability of developing a pit geometry capable creating local stress concentrations expected to initiate cracking, as will be discussed in the next section.

Efforts in FY18 will be primarily focused on creation and analysis of datasets developed from the currently running coupon exposures for up to one-year exposure duration. We will also expand on the environmental conditions of interest, including higher temperatures and cyclic humidity and temperature (representing the effect of diurnal variations in ambient weather on canister surface conditions). With regard to the latter, there is no information on how cyclic conditions expected on the canisters impact pitting kinetics; see Section 2.1 for further discussion. Conditions for these subsequent experiments will be determined based on our initial results from the current exposures. The resulting datasets and analysis will be distributed to our collaborators to inform and benchmark statistical and semi-deterministic canister cracking models currently under development at SNL, CSM and OSU. We will also communicate results in FY18 at relevant public conferences, including a paper presentation at the 2017 Electrochemical Society fall meeting.

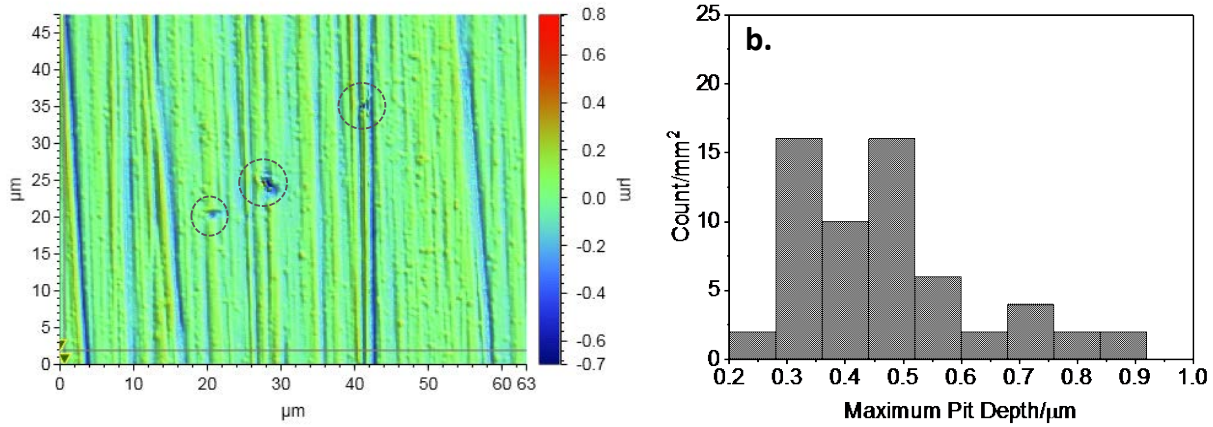

Figure 19. (a) Surface profile of "mill" finish 304L coupon exhibiting pits (circled) after humidity exposure and rust removal; (b) distribution of maximum pit depths measured across the surface of the same coupon. This coupon and others were loaded with 300 μg/cm^2 sea salt and exposed in a humidity chamber at 35°C, 75%RH for one week.

3.2 Pit-to-Crack Transition

In many susceptible alloys, corrosion pits are commonly observed as initiation sites for SCC cracks (see, for example Figure 20). Existing models for pit-to-crack transition relate pit size and shape to crack initiation through calculated stress intensity factors (Kondo, 1989; Turnbull et al., 2009; Horner et al., 2011). If the local stress intensity at the surface of a pit exceeds an empirically-determined SCC threshold stress (i.e., $K > K_{ISCC}$), a crack is assumed to initiate from that pit. The relevance of this relationship and accessible limits of these models, in general, are unknown for storage canister conditions. Furthermore, the validity of the assumption that general pit shape and size control pit-to-crack transition is not well understood. Other features, such as finer topography within pits (that could serve as stress concentrators) or microstructure could have a more commanding role in controlling pit-to-crack transition (Donahue and Burns, 2016). The aim of this work is to identify important features controlling pit-to-crack transition. Parameters of interest include pit shape, corrosion morphology (e.g. single versus satellite pits) and microstructure.

Our approach to understanding the controlling features for pit-to-crack transition and their prevalence under ISFSI-relevant conditions is to expose tensile test specimens of the same material as the coupon samples discussed in Section 3.1 to the same environmental conditions (salt load, T, and RH). During the period of exposure, the specimens will be held at a constant load with intermittent high R ripple fatigue loads applied to induce and track pit-to-crack transition. The ripple fatigue technique introduces marker bands along the crack front as it grows that can be followed, like tree rings, back to the point of crack initiation upon post-test SEM examination (Donahue and Burns, 2016). This approach will allow us to determine corrosion features that act as crack initiation sites along with the relative control of general pit shape and size. MicroCT and robotic serial sectioning are additional tools at Sandia we may utilize to further characterize these specimens. These experiments will enable us to rank relative importance of pit features within the specimens. Further experiments will be carried out where controlled pits are created in tensile specimens and then tested to refine these rankings. Assuming similar behavior between the tensile specimens and the exposed coupons, we will develop statistics on prevalence of these initiation-susceptible features with respect to exposure time and environment. These statistics could be used to validate the current pit-to-crack transition models based on stress intensity factor or be used in their place as input datasets for stochastic SCC models being developed by SNL, CSM and OSU.

This task initiated FY17Q2 and is being undertaken in collaboration with OSU and the WastePD EFRC program. Accomplishments in FY17 include preparation of tensile test specimens (304L and 316L) along with setup of environmental exposure chambers. Efforts in FY18 will focus on exposing these specimens under the same conditions as the current coupon exposures (see section 3.2) and identifying features controlling pit-to-crack transitions in the initial sample sets.

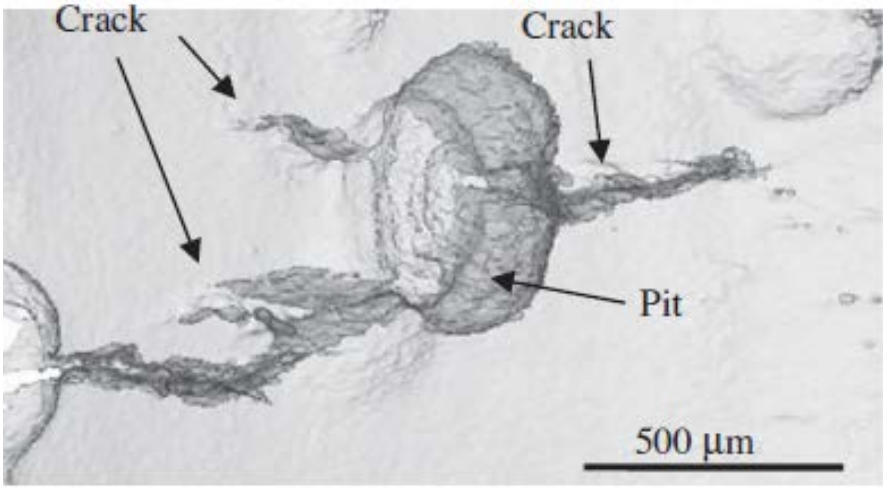

Figure 20. 3-D tomographic reconstruction of cracks emanating from a pit after exposure and mechanical loading of a 3 NiCrMoV disc. From (Horner et al., 2011).

3.3 Deterministic Linkage between Surface Environment, Damage Distributions and Rates

Confident extrapolation of stochastic canister SCC models utilizing environmental parameters as inputs and built on short term (e.g. several years) lab and field datasets to performance over decades requires mechanistic understanding of the environment-electrochemical relationship that drives pitting and SCC. Current deterministic models for atmospheric pitting and SCC provide insight into how surface environmental conditions can affect kinetics and extent of damage (Macdonald and Urquidi-Macdonald, 1991; Newman, 2002; Chen and Kelly, 2010). For example, in several SCC models, such as one proposed by Macdonald, the surface external to the crack acts as the cathode supplying the electrochemical driving force for crack growth, Figure 21. Thus, under atmospheric conditions, the surface environment (e.g., brine composition and thickness) would be expected to control damage rates. The relevance of these models as applied to SNF interim storage canisters remains largely unexplored. Furthermore, the relationship between surface state and electrochemical processes (e.g., reduction of oxygen) outside of a pit or a crack and electrochemical processes within them is not well understood. Efforts in this thrust aim to address this by quantitatively linking expected canister surface conditions to the electrochemical processes driving pitting and SCC, using existing models as initial basis for understanding.

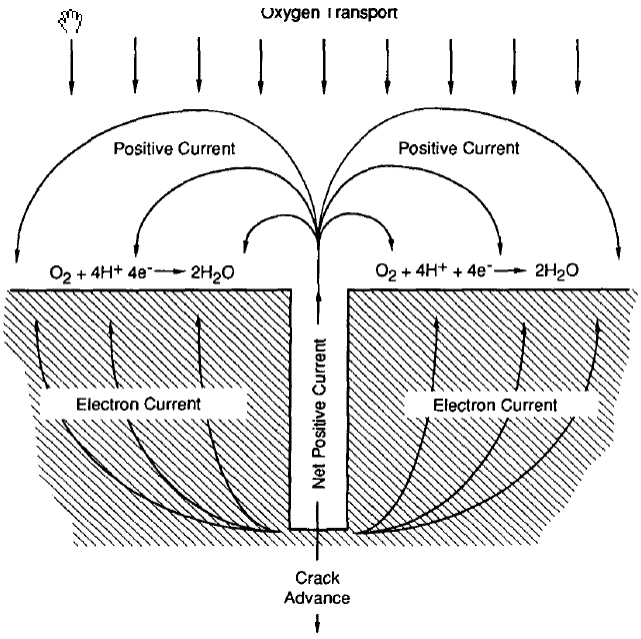

Figure 21. Conceptual schematic of physico-electrochemical SCC model proposed by MacDonald showing coupling of oxygen reduction reaction on steel surface with internal environment. From Macdonald and Urquidi-Macdonald (1991).

Of initial interest is the impact of expected surface electrolyte physicochemical state (See Section 2) on cathodic electrochemical kinetics that drive corrosion on stainless steel surfaces. In FY17Q2 we initiated experiments to measure the oxygen reduction reaction (ORR) kinetics on 304L in analog brines representative of chemistries and conditions expected on canisters. Oxygen reduction is the primary cathodic reaction driving corrosion processes on the canisters. To understand how electrolyte film thickness and chemistry impact the cathodic efficiency of the canister surfaces, we are measuring ORR kinetics on rotating disc stainless steel electrodes in simulated brine electrolytes. In these rotating disc experiments, the rotation speed of the electrode can be varied to control diffusion layer thickness, representative of atmospheric electrolyte layer thickness. Electrolyte layer thickness can be predicted from canister environmental parameters using the framework given in Section 2.

Rotating disc experiments were performed for SS 304 in a 1M NaCl solution for different rotation speeds (Ω) representing a range of electrolyte film thicknesses (δ). Cathodic polarization curves, shown in Figure 22, were obtained by scanning the potential from 0 to -1.5 V vs. SCE at 0.5mV/s for rotation speeds corresponding to environmental conditions. The potential at which the current density suddenly drops is the corrosion potential which ranged between -50 mV and -150mV. At potentials less than the corrosion potential there is a region where the current increases linearly with decreasing potential. This is referred to as the Tafel region in which the corrosion rate is inversely proportional to the slope of the polarization curve. At even less potentials, the current is no longer a function of potential as the reduction reaction is limited by mass transfer of oxygen to the surface. As the rotation speed is increased, the limiting current also increases. This plot demonstrates that increasing film thickness can lead to decreasing ORR rates in the oxygen diffusion limited regime. More experiments will be performed to study the effect of brine composition and temperature on the cathodic kinetics of 304 SS.

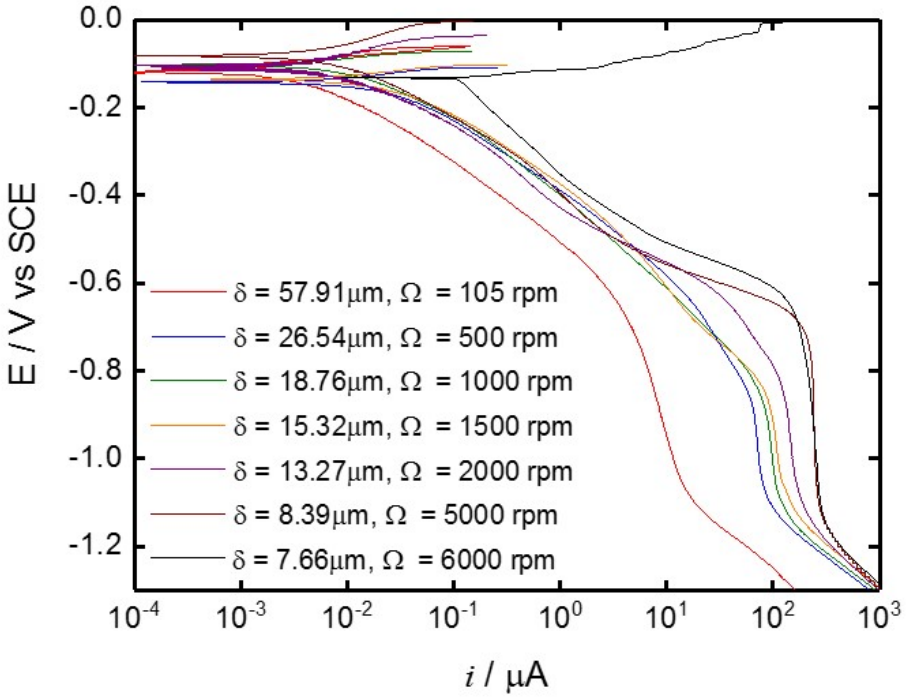

Figure 22. Cathodic polarization curves at varying electrode rotational speeds in 1 M NaCl solution at 21°C representing different brine layer thicknesses.

Using these data, the impact of varying surface environment on pitting damage is being explored via a maximum pit size model proposed by Chen and Kelly (2010). The premise of this model is that the physical and chemical properties of the brine that forms on the surface determines the maximum cathode capacity of the surface, which, in turn, can be used to determine the maximum size of a hemispherical pit that could be sustained by the cathode current.

Chen and Kelly (2010) derive the following equation for the maximum cathodic current available, $I_{c,max}$:

$$\ln I_{c,max} = \frac{4\pi k W_L \Delta E_{max}}{I_{c,max}} + ln\left[\frac{\pi e r_a^2 \int_{E_{corr}}^{E_{rp}} (I_c - I_p) dE}{\Delta E_{max}}\right] \quad \text{(Eq. 1)}$$

where

k = conductivity, Siemens/meter

W_L = brine layer thickness, meters

I_c = cathodic current density, Amps/m^2

I_p = passive current density, Amps/m^2 assumed to be 10^{-4} A/m^2 in Chen and Kelly

E_{rp} = repassivation potential = -0.4 V_{SCE} in Chen and Kelly for 304 = potential at the mouth of the pit

E_{corr} = -0.15 V_{SCE} in Chen and Kelly = E_L = potential at the cathode edge

e = Euler's number 2.71828

r_a = pit radius, meters

r_L = radius of the cathode, meters

$\Delta E_{max} = E_{corr} - E_{rp}$

Several of these parameters vary with the environmental conditions on the canister surface. These include the conductivity k, the concentration of salts in the brine m_{salt}, and the brine density ρ. These parameters vary with the RH at the canister surface. The RH is equal to the activity of water in the brine, and hence, controls the concentration of salts in the brine. The temperature has a relatively minor effect on brine concentration, but has a large effect on brine density and brine conductivity. For any given environmental (T, RH) condition, the brine volume varies linearly with the salt load deposition density.

The integral term on the right-hand side of the equation is determined from cathodic polarization curves, which will also potentially vary with brine layer composition and thickness. Chen and Kelly implemented a single cathodic polarization curve based on data for sea-water, measured by (Sridhar et al., 2004), and an anodic current based on the Galvele pit stability criterion. Further details and discussion of this model were reported in Bryan and Enos (2017).

We will implement the cathodic polarization curves that we have measured in the Chen and Kelly model to better understand the effect of brine composition and layer thickness on pit size. Figure 23 shows the impact of varying electrolyte thickness based, in part on data shown in Figure 22, on predicted maximum pit size. The dashed curves represent the maximum current provided by the cathode at a specific salt loading (SL) and electrolyte thickness for 1M NaCl, corresponding to a RH of about 97%. The solid lines correspond to the anode current required for pit stability calculated as I/r, which can range from 1-3 A/m for stainless steels (Scully et al., 1996; Moayed and Newman, 2006). The intersection between the anodic current required and the cathode current available predicts the maximum pit size achievable. The predicted maximum pit size decreases with increases in I/r, and increases as electrolyte layer thickness and RH increase.

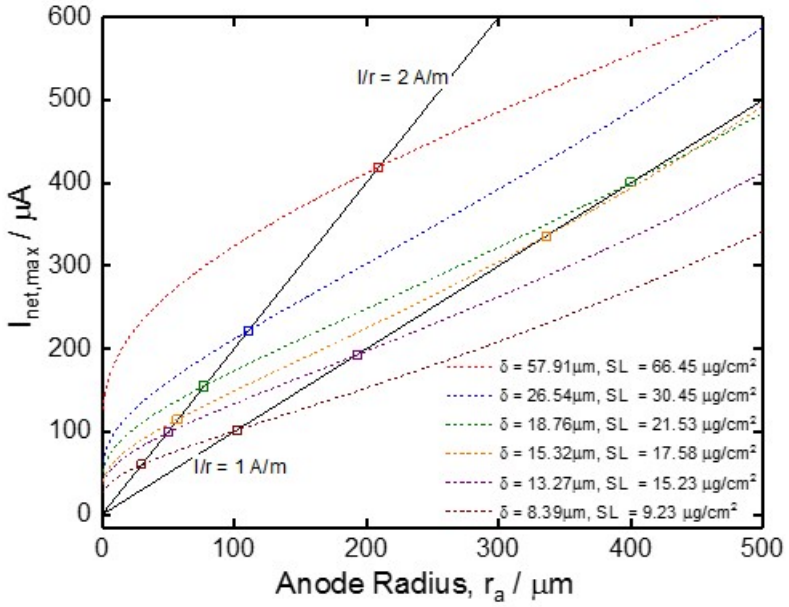

Figure 23. Effect of pit radius on cathode capacity (dashed lines) and anodic current demand (solid lines) predicted by Chen's maximum pit size model using the cathodic data presented in Figure 22. Symbols at curve intersections indicate predicted maximum pit radius under these conditions.

Critical combinations of environmental parameters at which there is a risk of SCC can be defined through the maximum pit size model and empirical measures of electrochemical kinetics. This model is currently utilized as part of SNL's SCC modeling efforts to determine bounding pit sizes on canisters as function of environment and surface salt loading. In turn, assuming Kondo criterion, these maximum pit sizes then

serve to determine conditions under which pit-to-crack transition would be most likely to occur. Similarly, conditions where cracking will not take place can also be determined. If the theoretical maximum pit size is smaller than the critical pit size required for SCC crack initiation (given the local stresses and environmental conditions that are present) then crack initiation is unlikely. Thus, if the environmental parameters and material properties for a system are known, this model can be used to map regions where there is a risk of SCC, requiring more detailed experimentation. Although of great potential utility, this model has not been benchmarked under canister-relevant conditions. It is likely that the model can only be implemented in a stochastic fashion, in which the likelihood of crack initiation increases with the predicted maximum pit size, but a minimum pit size that initiates a crack may not exist, or may be very small.

There are several assumptions in the maximum pit size model that may result in a non-conservative conclusion and that must be addressed. These include treating the pits as hemispherical in shape, the brine layer as a uniform thin film with static properties, and assuming the material and mechanical environment (e.g., stress/strain) is homogenous. In all cases, experimental data on distribution of pit geometries at the coupon level and on the canister mock-up is critical along with understanding the effect of dynamic environment on this distribution. Regarding the latter, it is given that canister cooling, seasonal and diurnal weather cycles, continuous deposition of atmospheric particles, and reactions with atmospheric gases, result in a highly dynamic brine system (see Section 2). Furthermore, corrosion processes can quickly (within minutes) and dramatically change the brine chemistry. For example, we and others have demonstrated that surface chemistry at cathode sites tends towards high alkalinity due to the ORR reaction producing hydroxyl ions, and, in turn carbonates due to reaction with atmospheric CO_2 (Schindelholz et al., 2014). Changing electrolyte properties could have considerable impact on both anodic and cathodic kinetics.

To understand the extent to which brine evolves on the surface and how, in turn, this evolution can impact cathodic corrosion kinetics, we are using surface sensitive analytical methods to map chemistry on coupons during the exposure experiments detailed in Section 3.1. Figure 24 shows the chemistry distribution on a salt-deposited coupon before exposure and after one month high humidity exposure as measured by TOF-SIMS. In these images, the irregular Na-enriched outlines represent the extent of the deliquesced droplets, while the circular droplets represent the dried droplets after removal from the RH chamber. The presence of discrete deposits makes it clear that the deposits remained as discrete deliquesced droplets as opposed to thin films. The diffuse outlines of the droplets after exposure indicates that NaCl is diffusing out from these droplets over time. These results suggest that the salt deposits deliquesce as droplets connected by thin, adsorbed water layers. The impact of this non-uniform brine geometry on predicted maximum pit depths will be explored in FY18. Alkaline signatures (OH^-, CO_3^{2-} and derivatives) indicative of cathodic areas were not detectable (detection limit ~ 1 part per million atoms) on these samples, nor were corrosion products visible in the analyzed areas. We hypothesize that, as corrosion develops, alkaline cathodic chemistry will become apparent and spread across the surface. Measures of cathodic kinetics in expected alkaline brine chemistries will be carried out in FY18 and their impact on maximum pit size assessed.

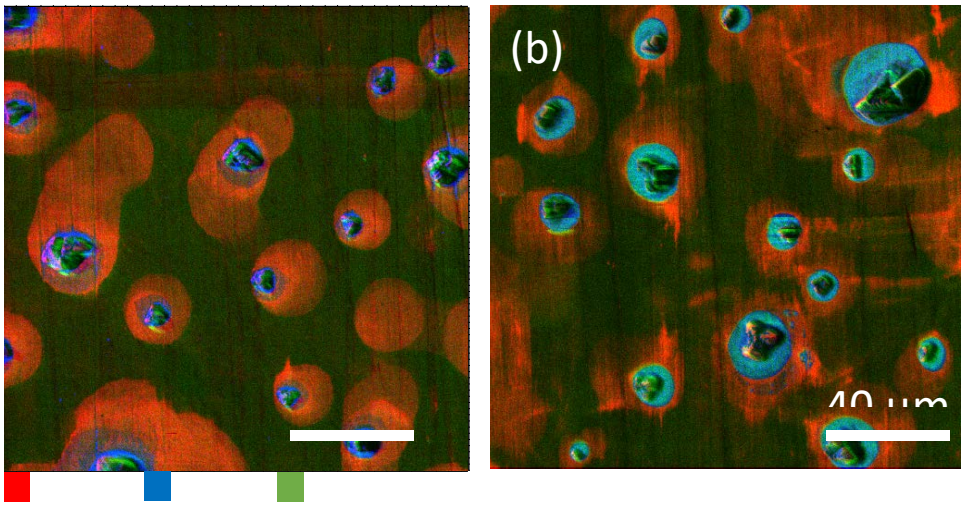

Figure 24. TOF-SIMS ion maps of sea salt deposits on 304L stainless steel before (a) and after (b) one month exposure at 35°C, 75%RH.

This page is intentionally left blank

4. RELATIONSHIP BETWEEN CORROSION DAMAGE, MATERIAL, AND MECHANICAL ENVIRONMENT

Quantitative information on the effect of material characteristics and mechanical environment (microstructure, composition, applied stress) on pitting damage distributions and rates, conditions of pit-to-crack transition, and crack growth are lacking under canister-relevant environments. The impact of variance of these material and mechanical environment parameters, within ranges present in canister materials, on model predictions is not well understood. This thrust aims to develop deeper understanding on how material variance impacts electrochemical corrosion processes related to SCC and resulting damage distributions and rates. Current efforts are focused on providing and electrochemical knowledge basis complimentary to experiments being carried out at CSM as part of IRP activities in this area.

Work in FY17 focused on setting up initial experiments to examine how static stress loads expected in the canister affect the pitting susceptibility of 304L. The goal is to (a) determine the relative importance of stress as a parameter in pitting susceptibility of the canisters and (b), if deemed relevant, develop a model to predict pitting susceptibility as function of stress with correlation to CSM results from 4-point bend specimen exposures in laboratory conditions and at the Maine Yankee site. A subset of preloaded 4-point bend specimens has been obtained from CSM, along with mapped stresses in the specimens as determined by digital image correlation (Figure 25). Microelectrochemical mapping techniques, such as the microcapillary configuration in Figure 26, will be used to map electrochemical behavior in regions of different stress on the specimen. Current efforts are focused on completing construction of the microcapillary mapping system that will be used for this work. This system will be used in FY18 to create electrochemical maps of the 4-point bend specimens and correlate behavior to stress. These results and associated analysis be utilized to interpret pit distributions and kinetics observed on exposed CSM samples of the same type.

An area of future work in this area is building an electrochemical description of weld zone regions on the canister for prediction of pitting and SCC susceptible zones and informing or updating models under construction. In FY18 we will expose a salt-loaded portion of the mockup canister to elevated temperature and humidity and subsequently map pitting and cracking frequency as related to microstructure and stress/strain. This will provide a general idea of most susceptible regions of the canister and how they relate to material variation and mechanical environment. During post-mortem analysis we will also attempt to identify pit-to-crack transition features, if apparent. This dataset can be used to further inform and benchmark models under development and guide experimental efforts.

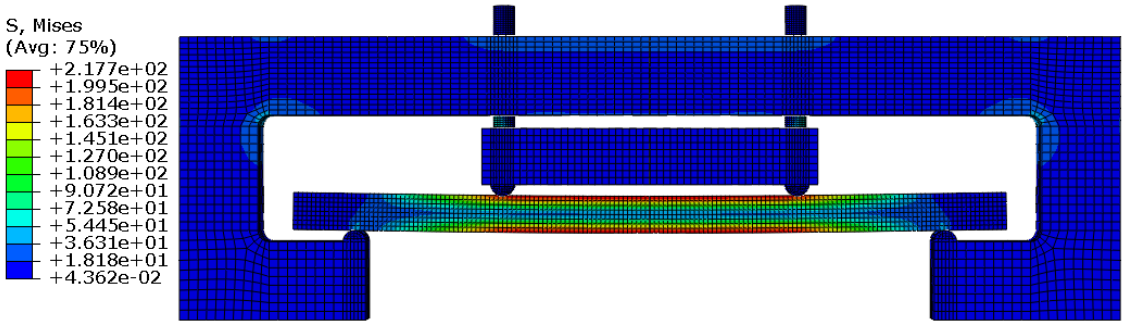

Figure 25. Stress map of test specimen in 4-point bend fixture, measured using differential image correlation.

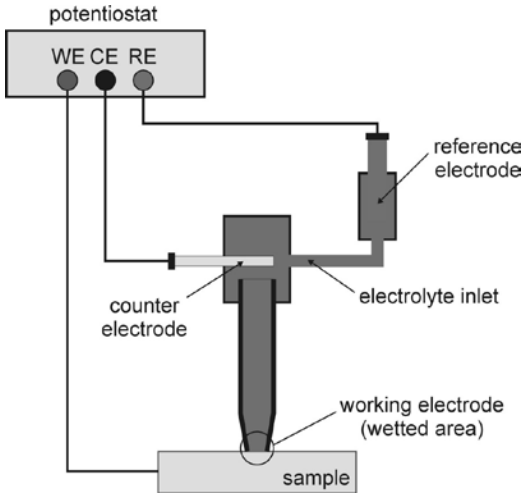

Figure 26. Schematic of microelectrochemical mapping system that will be used to map electrochemical behavior of 4-point bend specimens. From Andreatta and Fedrizzi (2016).

5. CONCLUSIONS

This progress report describes work done in FY17 at Sandia National Laboratories (SNL) to assess the localized corrosion performance of container/cask materials used in the interim storage of spent nuclear fuel (SNF). Of particular concern is stress corrosion cracking (SCC), by which a through-wall crack could potentially form in a canister outer wall over time intervals that are shorter than possible dry storage times. Work in FY17 refined our understanding of the chemical and physical environment on canister surfaces, and evaluated the relationship between chemical and physical environment and the form and extent of corrosion that occurs. The SNL corrosion work focused predominantly on pitting corrosion, a necessary precursor for SCC, and process of pit-to-crack transition; it has been carried out in collaboration with university partners. SNL is collaborating with several university partners to investigate SCC crack growth experimentally, providing guidance for design and interpretation of experiments.

Work to define the chemical and physical environment that could develop by deliquescence of sea-salts on storage canister surfaces consisted of thermodynamic modeling and experimental work to evaluate brine compositions and properties (e.g., volume as a function of relative humidity). These parameters are important inputs for mechanistic models of localized corrosion, such as that developed by Chen and Kelly (2010), and for stress corrosion cracking. However, the thermodynamic calculations do not consider reactions between atmospheric gases and sea-salt aerosol particles, known as gas-to-particle conversion reactions, that can significantly modify salt and brine compositions. One such reaction that could occur when sea-salts initially deliquesce to form magnesium-chloride-rich brines is carbonation—absorption of CO_2 from the atmosphere, coupled with concomitant outgassing of HCl and precipitation of non-deliquescent magnesium carbonate. Experimental evaluation of $MgCl_2$ brine stability at canister-relevant RH and temperature conditions confirmed that this reaction can occur, and could lead to rapid dry-out of the deliquesced brine. While acidification reactions with other atmospheric gases (e.g., HNO_3, H_2SO_4) may play a larger role in natural systems, the carbonation reaction is bounding. In experimental systems containing small masses of salts and run for long periods of time, understanding the role of atmospheric reactions, including the carbonation reaction, is critical for proper interpretation of the results. Consideration of atmospheric exchange reactions is critical to understanding the long-term stability of deliquescent brines on heated canister surfaces, and to judging the relevance of long-term corrosion experimental work in confined-volume laboratory systems.

Finally, work by other researchers has suggested that corrosion may be more extreme in natural environments due to daily and seasonal variations in temperature and RH, especially if the RH variations cross the deliquescence RH of the salts. Sandia will evaluate the effects of cyclic variations experimentally. However, on canister surfaces, the diurnal variations in the ambient temperature and RH will be modified by the decay heat of the canister. In preparation to running corrosion experiments under cyclic conditions, one realistic cycle for canister surface temperature and RH has been identified, and will be used in future experiments.

Sandia also initiated several experiments evaluating pitting corrosion and SCC under conditions relevant to the canister surface. These experiments focus on identifying the role of environmental factors (temperature, RH, and salt load) on the rate and extent of pitting damage over time. The first experiment aims to quantify pitting rates and size distributions over time on 304 stainless steel coupons, as a function of temperature, RH, and salt load, and is being carried out in collaboration with Ohio State University. Data from early sample pulls has been collected, and interpretation is underway. Features associated with pits that serve as crack initiation sites are also being identified as means of understanding what conditions initiate cracking. A second set of experiments is evaluating the kinetics of cathodic reactions as a function of brine layer thickness, composition, and temperature, using a high-speed rotating disc electrode. These experiments will provide needed inputs to mechanistic models that evaluate the maximum possible pit size that can form under a given set of environmental conditions. A third suite of experiments is evaluating the effects of the corrosion reactions on the distribution and composition of

solutes in the cathode region on the metal surface. Existing mechanistic models for corrosion largely ignore these effects, which can have a huge effect on brine compositions in the cathode region, potentially changing the kinetics of the oxygen reduction reaction. However, these reactions may also serve to disperse solutes over the metal surface, helping individual sea-salt particles form a continuous brine film. Finally, in collaboration with the Colorado School of Mines, Sandia is evaluating the effect of stress on pit size and shape distributions and the extent of damage. This is being done by evaluating pitting in stress profiles on the side of 4-point bend specimens aged under similar environments as our coupon pitting experiments. Colorado School of Mines has modeled the stress profiles, while Sandia will characterize the electrochemical properties of the metal as a function of location (and stress level) on the samples. This will ultimately provide information on the likely location of pits that initiate SCC on canister surfaces.

All of these experiments will extend into FY18, along with new experiments that will evaluate pitting, crack initiation, and crack orientation on samples from the Sandia full-dimeter canister mockup. The mockup experiments will provide a critical link between the laboratory-scale coupon experiments and actual corrosion on a spent nuclear fuel storage canister surface.

6. REFERENCES

Andreatta, F. and Fedrizzi, L. (2016). The use of the electrochemical micro-cell for the investigation of corrosion phenomena. *Electrochimica Acta* **203**, 337-349.

ASTM International. (2008). *D1141-98: Standard Practice for the Preparation of Substitute Ocean Water*. American Society for Testing and Materials, p.

Bryan, C. and Enos, D. (2017). *FY16 Status Report: SNF Interim Storage Canister Corrosion and Surface Environment Investigations.* FCRD-UFD-2016-00429. U.S. Department of Energy, 86 p.

Bryan, C. R. and Enos, D. (2014). *Analysis of Dust Samples Collected from Spent Nuclear Fuel Interim Storage Containers at Hope Creek, Delaware, and Diablo Canyon, California.* Sandia National Laboratories, 281 p.

Burstein, G. and Pistorius, P. (1995). Surface roughness and the metastable pitting of stainless steel in chloride solutions. *Corrosion* **51**, 380-385.

Chen, Z. and Kelly, R. (2010). Computational modeling of bounding conditions for pit size on stainless steel in atmospheric environments. *Journal of the Electrochemical Society* **157**, C69-C78.

Crisp, T. A., Lerner, B. M., Williams, E. J., Quinn, P. K., Bates, T. S. and Bertram, T. H. (2014). Observations of gas phase hydrochloric acid in the polluted marine boundary layer. *Journal of Geophysical Research: Atmospheres* **119**, 6897-6915.

Deelman, J. (1999). Low-temperature nucleation of magnesite and dolomite. *Neues Jahrbuch Fur Mineralogie Monatshefte*, 289-302.

Donahue, J. R. and Burns, J. T. (2016). Effect of chloride concentration on the corrosion–fatigue crack behavior of an age-hardenable martensitic stainless steel. *International Journal of Fatigue* **91**, 79-99.

dos Anjos, A. P. A., Sifeddine, A., Sanders, C. J. and Patchineelam, S. R. (2011). Synthesis of magnesite at low temperature. *Carbonates and Evaporites* **26**, 213.

Engelhardt, G. and Macdonald, D. D. (2004). Unification of the deterministic and statistical approaches for predicting localized corrosion damage. I. Theoretical foundation. *Corrosion Science* **46**, 2755-2780.

Enos, D. and Bryan, C. (2016). *Final Report: Characterization of Canister Mockup Weld Residual Stresses.* FCRD-UFD-2016-000064. U.S. DOE, 62 p.

EPRI. (2011). *Extended Storage Collaboration Program (ESCP) Progress Report and Review of Gap Analyses.* Technical report no. 1022914. p.

EPRI. (2015). *Susceptibility Assessment Criteria for Chloride-Induced Stress Corrosion Cracking (CISCC) of Welded Stainless Steel Canisters for Dry Cask Storage Systems.* 3002005371. Electric Power Research Institute, 206 p.

Eugster, H. P., Harvie, C. E. and Weare, J. H. (1980). Mineral equilibria in a six-component seawater system, Na-K-Mg-Ca-SO 4-Cl-H 2 O, at 25 C. *Geochimica et Cosmochimica Acta* **44**, 1335-1347.

Hanson, B., Alsaed, H., Stockman, C., Enos, D., Meyer, R. and Sorenson, K. (2012). *Gap analysis to support extended storage of used nuclear fuel.* U.S. Department of Energy, p.

Harris, G., Klemp, D. and Zenker, T. (1992). An upper limit on the HCl near-surface mixing ratio over the Atlantic measured using TDLAS. *Journal of atmospheric chemistry* **15**, 327-332.

Harvie, C. E., Weare, J. H., Hardie, L. A. and Eugster, H. P. (1980). Evaporation of seawater: calculated mineral sequences. *Science* **208**, 498-500.

Horner, D., Connolly, B., Zhou, S., Crocker, L. and Turnbull, A. (2011). Novel images of the evolution of stress corrosion cracks from corrosion pits. *Corrosion Science* **53**, 3466-3485.

Kondo, Y. (1989). Prediction of fatigue crack initiation life based on pit growth. *Corrosion* **45**, 7-11.

Kulmala, M., Toivonen, A., Mattila, T. and Korhonen, P. (1998). Variations of cloud droplet concentrations and the optical properties of clouds due to changing hygroscopicity: A model study. *Journal of Geophysical Research: Atmospheres* **103**, 16183-16195.

Macdonald, D. and Engelhardt, G. (2010). 2.39 Predictive Modeling of Corrosion. *Shreir's Corros, Elsevier BV*.

Macdonald, D. D. and Urquidi-Macdonald, M. (1991). A coupled environment model for stress-corrosion cracking in sensitized Type-304 stainless-steel in LWR environments. *Corrosion Science* **32**, 51-81.

McCaffrey, M., Lazar, B. and Holland, H. (1987). The evaporation path of seawater and the coprecipitation of Br^- and K^+ with halite. *Journal of Sedimentary Research* **57**, 928-937.

Moayed, M. H., Laycock, N. and Newman, R. (2003). Dependence of the critical pitting temperature on surface roughness. *Corrosion Science* **45**, 1203-1216.

Moayed, M. H. and Newman, R. (2006). The relationship between pit chemistry and pit geometry near the critical pitting temperature. *Journal of the Electrochemical Society* **153**, B330-B335.

Möller, D. (1990). The Na/Cl ratio in rainwater and the seasalt chloride cycle. *Tellus B* **42**, 254-262.

Newman, J. and Raju, I. (1981). An empirical stress-intensity factor equation for the surface crack. *Engineering Fracture Mechanics* **15**, 185-192.

Newman, J. C. and Raju, I. S. (1979). *Analysis of Surface Cracks in Finite Plates Under Tension or Bending Loads.* NASA, p.

Newman, R. C. (2002). Stress-corrosion cracking mechanisms. *CORROSION TECHNOLOGY-NEW YORK AND BASEL-* **17**, 399-450.

Nishikata, A., Ichihara, Y., Hayashi, Y. and Tsuru, T. (1997). Influence of electrolyte layer thickness and pH on the initial stage of the atmospheric corrosion of iron. *Journal of the Electrochemical Society* **144**, 1244-1252.

NRC. (2012a). *Identification and Prioritization of the Technical Information Needs Affecting Potential Regulation of Extended Storage and Transportation of Spent Nuclear Fuel. Draft for comment.* U.S. NRC, 138 p.

NRC. (2012b). *Potential Chloride Induced Stress Corrosion Cracking of Austenitic Stainless Steel and Maintenance of Dry Cask Storage System Canisters.* NRC Information Notice 2012-20, November 14, 2012. U.S. NRC, p.

NRC. (2014). *Assessment of Stress Corrosion Cracking Susceptibility for Austenitic Stainless Steels Exposed to Atmospheric Chloride and Non-Chloride Salts.* U.S. Nuclear Regulatory Commission, 173 p.

NWTRB. (2010). *Evaluation of the Technical Basis for Extended Dry Storage and Transportation of Used Nuclear Fuel.* NWTRB, 145 p.

Schindelholz, E. and Kelly, R. (2010). Application of inkjet printing for depositing salt prior to atmospheric corrosion testing. *Electrochemical and Solid-State Letters* **13**, C29-C31.

Schindelholz, E., Risteen, B. and Kelly, R. (2014). Effect of Relative Humidity on Corrosion of Steel under Sea Salt Aerosol Proxies I. NaCl. *Journal of the Electrochemical Society* **161**, C450-C459.

Schindelholz, E., Tsui, L.-k. and Kelly, R. G. (2013). Hygroscopic Particle Behavior Studied by Interdigitated Array Microelectrode Impedance Sensors. *The Journal of Physical Chemistry A* **118**, 167-177.

Scully, J., Pride, S., Scully, H. and Hudson, J. (1996). Some correlations between metastable pitting and pit stabilization in metals. *Critical Factors in Localized Corrosion II (ECS PV95-15), eds. P. Natishan, RG Kelly, G. Frankel, R. Newman (Princeton, NJ: The Electrochemical Society, 1996)*, 15.

Seinfeld, J. H. (1986). *Atmospheric Chemistry and Physics of Air Pollution*. New York, NY: John Wiley & Sons.

Siegel, J., Schindelholz, M. and Friedersdorf, F. (2015). Small Scale Crack Growth Sensor for Determination of AA5XXX Susceptibility to SCC. *CORROSION 2015*: NACE International.

SNL. (2007). *In-drift precipitates/salts model.* ANL-EBS-MD-000045 REV 03. Sandia National Laboratories, p.

Sridhar, N., Brossia, C., Dunn, D. and Anderko, A. (2004). Predicting localized corrosion in seawater. *Corrosion* **60**, 915-936.

Suffield, S., Fort, J. A., Cuta, J. M. and Adkins, H. E. (2012). *Thermal Modeling of NUHOMS HSM15 Storage Module at Calvert Cliffs Nuclear Power Station ISFSI.* U.S. Department of Energy, p.

Turnbull, A., Horner, D. and Connolly, B. (2009). Challenges in modelling the evolution of stress corrosion cracks from pits. *Engineering Fracture Mechanics* **76**, 633-640.

Turnbull, A., McCartney, L. and Zhou, S. (2006). Modelling of the evolution of stress corrosion cracks from corrosion pits. *Scripta materialia* **54**, 575-578.

Van't Hoff, J. H. (1905). *Zur Bildung zeanischer Salzblagerungen: 1st issue*: Vieweg.

Van't Hoff, J. H. (1909). *Zur Bildung zeanischer Salzblagerungen: 2nd ed*: Vieweg.

Van't Hoff, J. H. (1912). *Untersuchungen tiber die Bildungsverhaltnisse der ozeanischen Salzablagerungen*. Leipzig: Akad. Verlags ges.

Vierkorn-Rudolph, B., Bächmann, K., Schwarz, B. and Meixner, F. (1984). Vertical profiles of hydrogen chloride in the troposphere. *Journal of atmospheric chemistry* **2**, 47-63.

Wagner, W. and Pruß, A. (2002). The IAPWS formulation 1995 for the thermodynamic properties of ordinary water substance for general and scientific use. *Journal of physical and chemical reference data* **31**, 387-535.

Wolery, T. W. and Jarek, R. L. (2003). *Software User's Manual, EQ3/6 Version 8.0.* Sandia National Laboratories, p.